Design and Simulation of High Quantum Efficiency Segmented Waveguide Photodetector for Quantum Measurements

A Thesis

Presented to

the faculty of the School of Engineering and Applied Science

University of Virginia

In Partial Fulfillment of the

Requirements for the Degree of

Master of Science

by

Jie Pan

December 2023

APPROVAL SHEET

This Thesis

is submitted in partial fulfillment of the requirements

for the degree of

Master of Science

Author Signature: _____

This Thesis has been read and approved by the examining committee:

Advisor: Dr. Andreas Beling

Committee Chair: Dr. Joe C. Campbell

Committee Member: Dr. Kyusang Lee

Accepted for the School of Engineering and Applied Science:

Jennifer L. West, School of Engineering and Applied Science

December 2023

Design and Simulation of High Quantum Efficiency Segmented Waveguide Photodetector for Quantum Measurements

Abstract

The segmented waveguide photodetector has the potential to play a crucial role in quantum measurements, especially for photon number resolution. My findings reveal that the proposed segmented waveguide photodetector can exhibit extremely low loss performance once it is fully optimized.

In this study, I focus on the design and simulation of a segmented waveguide photodetector with high quantum efficiency, utilizing the eigenmode expansion (EME) in FIMMWAVE software. By utilizing the FDM (finite difference mode) Solver, I was able to model and simulate the device with precision, allowing me to optimize its design for optimal performance. Through optimization of the device design and comprehensive analysis of the quantum efficiency and loss mechanisms, I have achieved valuable results. The enhanced quantum efficiency makes it an ideal candidate for accurate photon number resolution in quantum measurements.

The detailed analysis of the quantum efficiency and loss mechanisms provides valuable insights into the underlying physics and mechanisms governing the device's performance. Through the analysis of a single PD cycle, optimizing the PD width, PD length, PD absorber thickness, and etching cladding layer depth, I was able to reduce the radiation loss to a level of 10^{-5}. This significantly enhanced the entire system's potential, eventually reaching up to 337 PDs. The final outcome reveals that the system of the 337 segment PDs except the first PD is with a total radiation loss of only 0.29% and the total quantum efficiency is 99.6%, which is already quite high, very close to 100%, suggesting that my optimization efforts have been highly successful. This substantially surpasses previous designs, elevating the optimization of reducing radiation loss to an exceptionally high level. This optimization can be leveraged to further improve the device and explore potential applications in quantum information processing and quantum communication.

Overall, this study presents an advancement in the design and simulation of high quantum efficiency segmented waveguide photodetector. The promising results obtained highlight the potential of this device for use in quantum measurements, paving the way for further advancements in the field of quantum technologies.

Acknowledgment

I would like to take this opportunity to extend my sincere gratitude to the individuals who have played a significant role in the success of this project and thesis.

First and foremost, I express our deepest appreciation to my thesis advisor, Prof. Andreas Beling. His unwavering support and guidance have been an immeasurable gift on this journey. Prof. Beling's counsel and willingness to lend an ear have been nothing short of blessings. His unwavering faith in my capability has given me the strength and courage to chase my dreams. His logical, evidence-based approach to problems has profoundly shaped my own thought process, a skill I believe is indispensable for advancing knowledge in my field.

I would also like to thank Professor Joe Charles Campbell and all the professors who have taught me, and the Assistant Manager for Administration and Student Services of ECE, Beth Eastwood-Beatty. Their dedication and support have been instrumental in making this scholastic endeavor a little easier. I am grateful for every letter written and every question answered. They are my heroes, and I owe a debt of gratitude to them.

My heartfelt thanks go to the members of my advising committee, Prof. Joe Charles Campbell, and Prof. Kyusang Lee. Their advice and insights have been invaluable in shaping my research. I have benefited from their teachings and guidance, gaining a deep understanding of the expectations of a superb research scientist.

To my fellow group members, Dr. Qianhuan Yu, Dr. Ta-ching Tzu, Junyi Gao, Xiangwen Guo, Masoud Jafari, Fatemeh Tabatabaei, Tasneem Fatema, Junwu Bai and Adam Dadey, I extend my gratitude for their assistance and being friendly research sounding board. Their support and camaraderie have made the research process more enjoyable. In particular, I would like to express my sincere gratitude to Dr. Qianhuan Yu for his previous efforts on this project. His dedication and contributions have been a constant source of inspiration and have provided me with a solid physical basis for my own research. I am grateful for his valuable insights and the knowledge he has shared, which have greatly influenced the direction and development of my work. His work has set a high standard, and I am fortunate to have had the opportunity to build upon his foundation.

Finally, I would like to acknowledge the university's computing center for providing us with access to the computational resources essential for my project's success. Their support has been invaluable, and I am grateful for the opportunities it has afforded us. I would also like to express my sincere gratitude to the FIMMWAVE software team and their support throughout this project.

To each person mentioned above, I convey my deepest appreciation for their contributions to my academic journey and the completion of this project. Their guidance, support, and expertise have left an indelible impact on my personal and professional growth. Last but not least, I would like to express my gratitude to my parents and girlfriend. Without them, I would not be able to achieve any accomplishments.

Table of Contents

List of Figures and Tables

Chapter 1. Introduction and Motivation

1.1 Objective

The main objective of this thesis is to realize a segmented waveguide photodetector design with high quantum efficiency (QE) tailored for the needs of a single-photon detection system based on the previous design [1-2]. Therefore, for simplicity in my work, I conducted research on various mainstream PD types and selected a monolithically integrated InP-based p-i-n segmented waveguide photodetector that is coupled to a single waveguide, and results can be applied to APDs and SPADs. I used the commercial software FIMMWAVE to fully optimize the structure, reducing radiation loss and enhancing quantum efficiency. Throughout this process, I analyzed the physical principles and parameter selections for each optimization, achieving an ultimately extremely low loss performance that can meet the requirements of quantum measurements. Furthermore, I proposed some ideas for future improvements in the segmented waveguide photodetector design.

1.2 Photodiode structure

Various photodiode structures have been developed to improve the responsivity, bandwidth of PD, APD gain and photon detection efficiency. The mainstream designs include the PIN, APD and SPAD structures.

1.2.1 PIN structure

The PIN structure is the simplest design of a photodiode with an intrinsic layer as the absorber. The traditional pin-type photodetector for 1550 nm consists of two heavily doped p-type and n-type wide-bandgap materials, forming a structure with an intrinsic $In_{0.53}Ga_{0.47}As$ light-absorbing layer in between, as depicted in the figure 1. When incident light enters the photodetector, it generates photogenerated electrons and holes in the absorption region. Under the influence of the reverse electric field, photogenerated electrons and holes move towards the n-electrode and p-electrode directions, respectively, resulting in photocurrent. In the case of a pin-type structure, the $In_{0.53}Ga_{0.47}As$ material serves as both the absorption region and the depletion region at the telecom wavelengths.
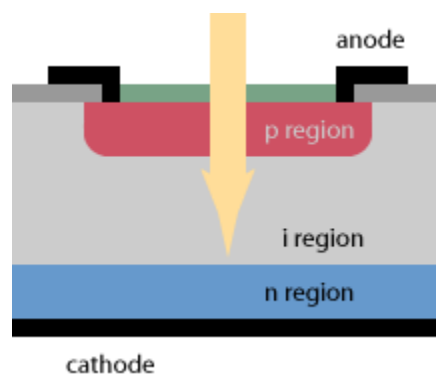
Figure 1. Schematic drawing of a p–i–n photodiode [3]

The quantum efficiency (QE) is a significant parameter that represents the efficiency of a photodiode to convert incident photons into electrons. The QE represents the electron-hole pairs per incident photon. For a PIN photodiode, the gain is typically 1, implying that ideally each incident photon creates a single electron-hole pair. Dark current, on the other hand, represents the current that flows when no light is incident on the photodiode and is essential for quantum applications. Elevated dark current can lead to an increase in noise, affecting the photodiode's ability to detect low-light levels accurately. Detecting single photons requires a very low noise floor, and given the inherent noise in PIN diodes due to their dark current and the lack of intrinsic gain, they're typically not suitable for single-photon detection applications.

1.2.2 APD structure

Avalanche photodiodes (APDs) stand out as distinct semiconductor entities designed to harness the avalanche multiplication effect in the linear regime, thus boosting the signal. At their core, APDs bear a resemblance to PIN diodes. However, a distinguishing factor is the region of high electric field in APDs, tailor-made to facilitate avalanche processes. Once a photogenerated carrier enters this region, it potentially accumulates sufficient kinetic energy to cause ionization of adjacent semiconductor atoms. This action precipitates the generation of secondary carriers, a phenomenon termed as impact ionization, as shown in the figure 2. The net effect is the amplification or gain of the photocurrent.
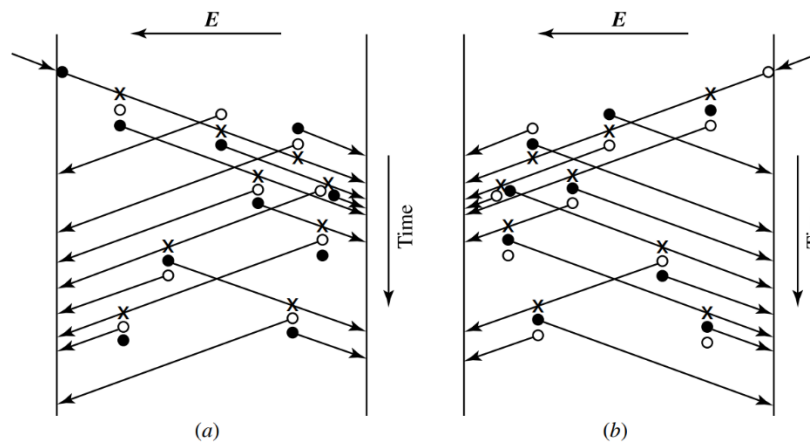
Figure 2. Avalanche multiplication of electrons and holes through impact ionization in a semiconductor in the presence of a high electric field with (a) electron injection in the case of $k < 1$ and (b) hole injection in the case of $k > 1$[4]

The salient advantage proffered by APDs over their PIN counterparts lies in their inherent capability for internal gain. This characteristic amplifies the diode's responsivity manifold. The degree of gain an APD can achieve is a function of the reverse bias voltage applied. This heightened sensitivity, however, comes with a caveat — an escalated noise level, described by an excess noise factor. This rise is primarily attributed to the avalanche noise, an offshoot of the intrinsically random nature of the avalanche process. Optimizing gain, excess noise, and other noise sources in the system becomes imperative for applications where signal clarity is paramount.

1.2.3 SPAD structure

Single photon avalanche diodes (SPADs) are specialized APDs, meticulously calibrated for the detection of individual photons. Operating on the Geiger mode principle, SPADs are biased surpassing

their breakdown voltage as shown in the figure 3(a) In scenarios where the SPAD absorbs a photon, this event can catalyze an avalanche breakdown. This reaction manifests as a pronounced current pulse, serving as a testament to the photon's presence. From the figure 3(b), it is easy to distinguish the gain versus reverse voltage curve for different PDs.
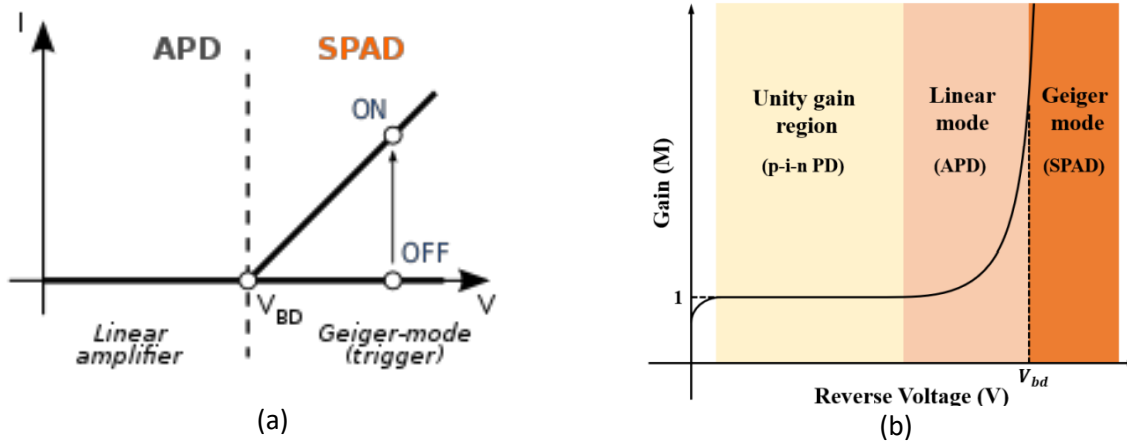
Figure 3. (a) Current-voltage characteristic of a SPAD showing the off- and on-branch[5] (b) Gain versus reverse voltage curve for different PDs[5]

The standout feature of SPADs is their exemplary photon detection efficiency (PDE) at the granularity of single photons. However, they are not without their challenges. An intrinsic attribute of SPADs is the "dark count"—a scenario where detection is erroneously signaled in the absence of actual photons, commonly due to factors like thermal carrier generation. Post each detection cycle, SPADs mandate a quenching mechanism, reinstating them to their operational state. This introduces a latency or "dead time," rendering the SPAD momentarily unresponsive to subsequent photon arrivals. Both the "dark count" metric and the "dead time" duration are pivotal factors delineating the efficacy of SPADs in quantum-centric applications.

1.3 Photodiode for photon counting

Photon counting is a fundamental and essential technique used in a wide range of scientific and technological applications. The process involves detecting and recording individual photons that strike a detector. The detection of photons relies on the principle of the photoelectric effect. When incident photons interact with the detector material, they cause the release of electrons or generate an electrical signal that is proportional to the energy of the photon.

One of the key advantages of photon counting is its ability to perform precise measurements and analysis of light sources with exceptionally low light levels. Additionally, it facilitates the exploration of quantum phenomena at the single-photon level. As a result, photon counting finds extensive application in various fields, including quantum optics, spectroscopy, astronomy, quantum information processing, and fluorescence imaging, among others. The quantification and analysis of individual photons provide researchers with valuable insights into the properties and behavior of light in these applications. The figure 4 shows some of the main application areas of the single-photon counting.
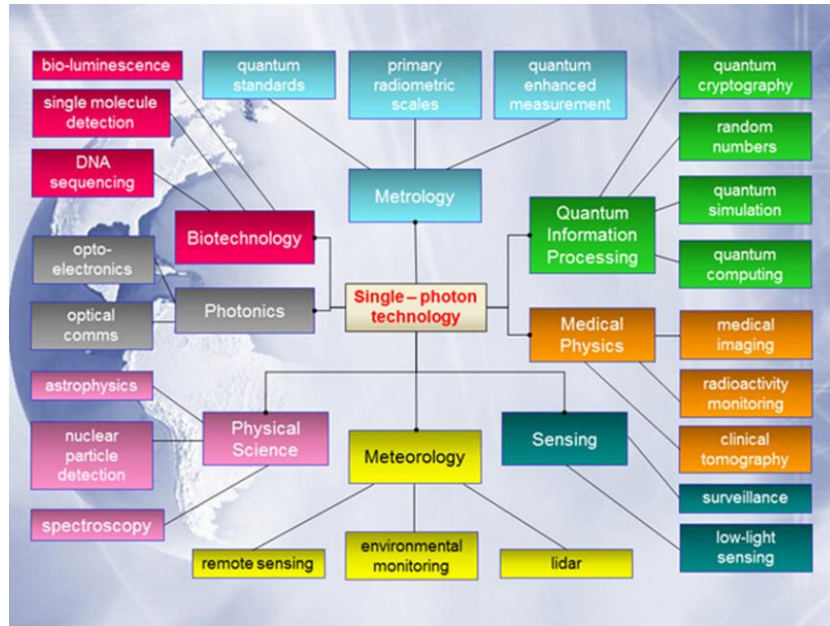
Figure 4. Main application areas for single-photon detection and generation [6]

Currently, commonly used single-photon detectors include photomultiplier tubes (PMT), single photon avalanche diode (SPAD), and superconducting nanowire single photon detector (SNSPD), the transition edge sensor (TES) which can detect single photons with PNR. These innovative photodetectors offer promising alternatives for single-photon detection and cater to various research and application needs.

1.3.1 PMT

The PMT is a traditional optoelectronic device used in single-photon technology. The PMT consists of components such as a photocathode, focusing electrodes, dynodes, and an anode, as shown in the figure 5. It is a vacuum-based photosensitive device capable of converting weak light signals into measurable electrical signals, operating on the principles of external photoelectric effect and secondary emission theory.
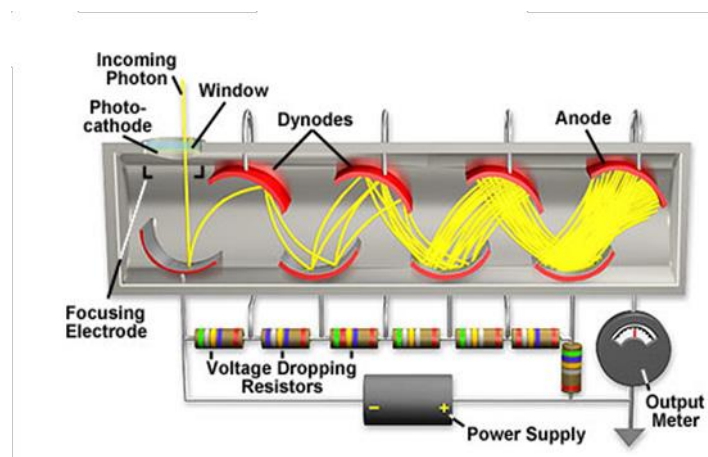
Figure 5. Typical Structure of a PMT [7]

4

When light illuminates the photocathode, it stimulates the emission of photoelectrons from the cathode due to the photoelectric effect. These emitted electrons are accelerated by an external electric field created by the focusing electrodes and enter the dynode system. By controlling the applied voltage across the dynodes, hundreds or even thousands of secondary electrons are released for each primary electron, resulting in significant amplification. Finally, the high-potential anode collects the amplified photocurrent, generating an anode current or voltage output. PMTs are indeed sensitive detectors of light, capable of detecting even individual photons. However, traditional PMTs are not inherently designed for photon number resolving (PNR). While they can certainly detect the presence of low-light levels or even single photons, discerning the exact number of incident photons, especially when they arrive nearly simultaneously, is challenging for a conventional PMT. That said, there are specialized PMTs and associated electronic setups that can provide some level of PNR capability by assessing the size of the detected current pulse, but they may not achieve the accuracy or efficiency of dedicated PNR detectors.

1.3.2 SPAD

Single-photon detectors operating in the communication wavelengths of 1310 nm and 1550 nm have extensive application demands in fields such as fiber optic communications, laser radar, quantum secure communications, and autonomous driving. Considering human eye safety, the 1550 nm short-wave infrared single-photon detector demonstrates broader applicability. Simultaneously, it poses urgent development requirements for single-photon detectors with high detection efficiency, high count rates, high-temperature operation, and low cost. The continuous improvements and developments in material structure, material quality, process preparation, and quenching circuits of InP/InGaAs short-wave infrared SPADs have significantly enhanced their performance shown in the figure 6. Many companies have successfully developed such single-photon detector products, including the SPAD series by Princeton Lightwave and the series by Hamamatsu Photonics, where the typical detection efficiency has increased from 20% to 30%, and the dark count rate has been further reduced to below kHz.
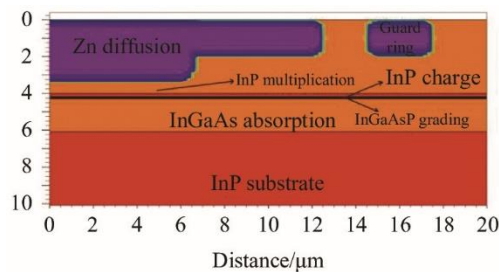
Figure 6. Schematic diagram of InP/InGaAs SPAD [8]

For 1550 nm single-photon detection technology, apart from traditional InP/InGaAs SPADs, new materials, structures, and mechanisms have been explored. These include low-noise material systems constructed with Sb-based digital alloys, multiple gain InP/InGaAs SPADs utilizing ion implantation, single-chip integrated thin-film resistor-based negative feedback self-quenching (NFAD) SPADs, InAlAs/InGaAs SPADs, among others [8]. These advancements have led to rapid progress and development in single-photon detection chip technology.

Photon detection efficiency (PDE) is a crucial metric for photodetectors, as it characterizes the device's capability to detect light. This efficiency is the product of several factors, including quantum efficiency, the probability of injecting holes or electrons into the multiplication region, the probability of

triggering avalanche in the multiplication layer, and the probability of detecting the avalanche. Consequently, enhancing the device's quantum efficiency can improve the overall detection efficiency. In 2012, Milan Polytechnic University [9] reported a modification to the existing SAGCM structure by adding a 200 nm SiNx anti-reflection coating optimized for 1550 nm photons. This coating reduces photon reflection and boosts quantum efficiency. Under 5 V over-bias and at 200 K, the relationship between the detection efficiency and different wavelengths is shown in the figure 7. For light at 1550 nm wavelength, the detection efficiency is >25%, while for light at 1000 nm wavelength, the PDE is 40%.
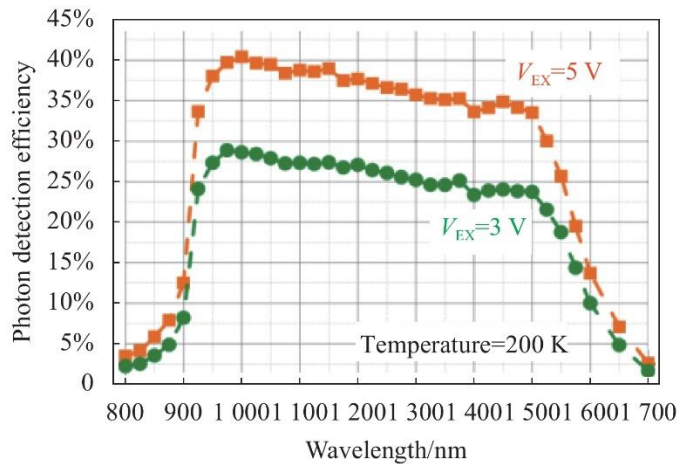
Figure 7. Relationship between different light wavelengths and SPAD detection efficiency from Politecnico di Milano [9]

1.3.3 SNSPD

Devices built on PMT are primarily tailored for efficient single-photon detection within the visible light spectrum. As technology advanced, the emergence of InGaAs/InP-based SPADs extended the detection capabilities to encompass the near-infrared spectrum. However, when compared to their counterparts designed for visible light, their performance is noticeably lower. They are confronted with low count rates, pronounced time jitter, and notably, the problematic issue of dark counts. Dark counts, which represent the noise due to the detection of spurious signals in the absence of incident photons, present a significant concern for precision measurements.
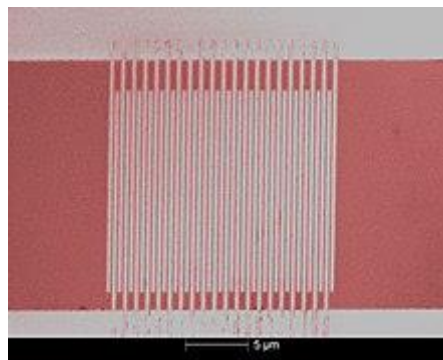
Figure 8. False-color scanning electron micrograph of a superconducting nanowire single-photon detector (SNSPD). Image credit: NIST. [10]

The superconducting nanowire single-photon detector (SNSPD) offers an alternative. It functions based on the superconducting transition of a nanowire: when a photon is absorbed, it disrupts the superconducting Cooper pairs, eliciting a discernible electrical signal. Among their standout features,

SNSPDs have a remarkable quantum efficiency, often breaching the 90% threshold, and they respond at breakneck speeds, typically in the picosecond domain. These characteristics position them favorably for photon number resolution tasks. Another feather in their cap is the notably low dark count rate, ensuring their viability in high-photon flux scenarios. However, the broader adoption of SNSPDs is still constrained by a couple of pivotal challenges: the mandate for operations at extremely low temperatures, below 4 K, and the intricate nature of their readout electronics.

In 2001, Goltsman et al. [11] fabricated a superconducting nanowire approximately 5 nm thick and 200 nm wide from NbN, successfully achieving visible light and near-infrared ultrafast single-photon detection and counting. This breakthrough laid the foundation for the subsequent research on superconducting nanowire single-photon detectors (SNSPDs). Through further research on SNSPD materials and detection principles, SNSPDs demonstrated significantly superior comprehensive performance metrics in the near-infrared spectrum compared to other types of single-photon detectors. In 2009, Robert Hadfield et al. [12] outlined the significant progress made in SNSPD detection technology and its impact on the fields of quantum optics and quantum information. In 2012, Natarajan et al. [13] summarized the improvements in SNSPD device performance, practical cooling techniques, optical coupling schemes, and applications in a systematic manner. In 2021, Esmaeil Zadeh et al. [14] provided a review of the developmental history, working mechanisms, manufacturing methods, superconducting materials, readout approaches, and prospects for low-temperature device integration of SNSPDs. With the continuous advancement of SNSPDs, their detection efficiency at a working wavelength of 1550 nm now exceeds 90%, far surpassing other types of detectors in detection efficiency.

1.3.4 TES

The transition-edge sensor (TES) is a photon detection device known for its ability to detect single photons with photon-number resolution. Comprising two transition-edge sensors made of tungsten chips, the TES is cooled to a stable temperature of 100 mK. Upon the incidence of a photon, the tungsten chip absorbs its energy, leading to a sharp increase in resistance. This alteration in resistance generates a pulse in the TES current, which is then detected by an inductively coupled SQUID amplifier. Operating in the superconducting temperature range, the TES demonstrates a linear relationship between resistance and temperature, thereby enabling it to achieve photon-number resolution for up to 5 photons. This characteristic makes the TES ideally suited for accurate measurements of photon numbers in the superconducting regime.
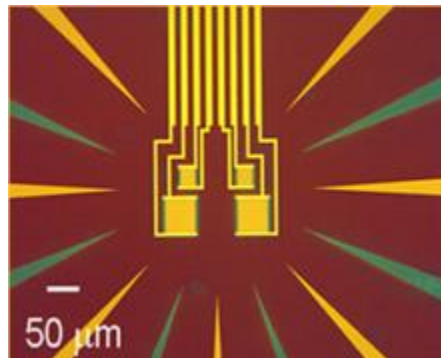
Figure 9. Optical image of four tungsten transition-edge sensors for near-infrared single-photon detection. Image credit: NIST [15]

One of the primary advantages of TES is its high sensitivity, enabling it to detect single photons with remarkable efficiency. Additionally, TES exhibits a fast response time on the order of 100 ns, allowing for prompt detection of photons. The linear behavior of TES, exemplified by its resistance-temperature relationship, facilitates accurate measurements of photon numbers. Moreover, TES's operation in the superconducting temperature range results in improved signal detection and resolution.

However, TES also presents certain disadvantages. Firstly, it necessitates cooling to a stable temperature of 100 mK, requiring the use of an adiabatic demagnetization fridge and specialized equipment, making the setup complex and maintenance-intensive. Secondly, TES has limitations regarding photon flux, with a maximum sustainable photon flux of 5 photons/μs in the continuous-wave regime, thereby limiting the maximum photon flux that it can effectively detect. Additionally, TES can be sensitive to noise, necessitating careful calibration and filtering to ensure accurate detection. Lastly, the TES system involves a complex setup with cryostats, tungsten chips, and inductively coupled SQUID amplifiers, setting it apart from other photon detectors in terms of complexity.

In conclusion, the transition-edge sensor offers high sensitivity and fast response time, making it well-suited for detecting single photons with photon-number resolution. Nevertheless, it requires specialized cooling and has certain limitations concerning photon flux and sensitivity to noise.

1.4 PDs for photon number resolution

The term "photon-number-resolving" is commonly used to describe a photon-counting detector capable of determining the number of simultaneously-incident photons, even if the detector cannot differentiate between photons incident simultaneously and those closely spaced in time. Photon-number-resolution without precise timing finds applications in various research efforts, including linear optics quantum computing, conditional state preparation, and source characterization for enhanced quantum-key-distribution security [16]. However, photon-number-resolving detectors with precise timing could prove beneficial in other applications that employ photon counting detectors, such as high-sensitivity optical communication, laser radar, and fluorescence measurement techniques [17], particularly if the ability to resolve and time multiple photons allowed dead-time effects to be mitigated. Unfortunately, most proposed and demonstrated photon-number-resolving detectors currently achieve photon number resolution at the expense of high timing jitter and low counting rate. A photon-number-resolving detector with speed and timing resolution matching or surpassing the best available for single-photon detectors would significantly enable many systems requiring high-speed performance. The intrinsic noise in the detector — most notably, the noise due to the gain variation — can affect the output enough to create uncertainty as to the number of impinging photons. The figure 10 shows this in detail.
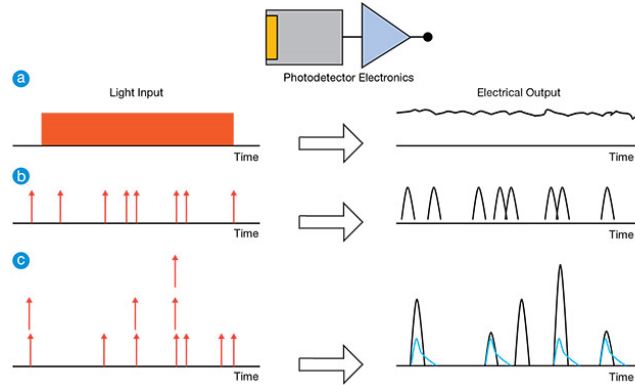
Figure 10. Three different input light conditions (left) and the corresponding detector outputs (right). Analog detection, in which the output is a continuous function of, for example, voltage as a function of time (a). Photon counting, where the input consists of individually arriving photons and the output of the corresponding electrical pulses (b). The responses of binary (blue) and proportional (black) detectors in response to multiphoton input delta pulses (c). Courtesy of Hamamatsu [18].

The first of two approaches to achieving photon-number-resolution is by using a linear-mode detector with sufficiently low noise, allowing the number of simultaneously detected photons to be resolved by measuring the amplitude of the resulting output signal. Several detector technologies capable of resolving photon number in this manner have been demonstrated, including visible light photon counters, superconducting transition edge sensors, and superconducting tunnel junction detectors. The fidelity with which a photon-number measurement can be made using these devices is limited by both non-unity detection efficiency and the signal-to-noise ratio of the output signal. This fidelity progressively worsens in distinguishing between n and n+1 photons as n becomes large. While these technologies exhibit high detection efficiency and are excellent for measuring the photon-number statistics of low-rate, pulsed sources, measuring non-pulsed sources is more challenging. If photons do not arrive in well-separated pulses over time, resolving detection events that occur while the detector is recovering from a previous event becomes a complex problem, and the measurement result can depend strongly on not only the detector but also the readout electronics.

The second approach for achieving photon-number-resolution is by splitting the light between many spatial or temporal modes, ensuring that each mode contains much less than 1 photon on average. Each of these modes is then separately measured using single-photon-sensitive detectors whose outputs can be digitally combined.

While a more significant number of detectors might intuitively seem advantageous, Rajveer Nehra's paper [2] delineates the requisite number of detectors based on the targeted photon detection count. He carried out the theoretical evaluation of the photon-count Positive-Operator-Valued Measures (POVMs) for a segmented detector which was designed by Qianhuan Yu. Results show that PNR detection in the ideal case of no losses and no dark counts requires on the order of 10^3 SPADs to resolve 10 photons, using an efficient gradient coupling scheme. Each individual detector should be characterized by minimal absorption and radiation losses, a precisely determined QE, and the overarching goal is to refine the system's high total QE to ensure high performance.

1.5 Waveguide photodiode

High-speed and high-quantum-efficiency photodiodes (PDs) are fundamental components in a wide range of applications, including optical communications, sensing, and microwave photonics. These devices are crucial for converting incoming optical signals into electrical signals with high speed and sensitivity.

One of the primary challenges in conventional normal incidence PDs is the well-known bandwidth-efficiency trade-off. As the bandwidth of a PD increases, its efficiency tends to decrease, and vice versa. To overcome this limitation, researchers have developed alternative designs such as side-illuminated or waveguide-photodiodes. These waveguide PDs offer distinct advantages over their conventional counterparts.

Waveguide photodiodes function by channeling the optical signal through a structured waveguide instead of allowing it to directly strike the absorber layer. This unique configuration facilitates enhanced responsivity and a truncated carrier transit time, owing to the non-collinear nature of the electrical and optical transports. Consequently, waveguide PDs are poised to deliver swifter response durations and an elevated quantum efficiency. These attributes render them particularly apt for high-speed optical communications and an array of other domains necessitating prompt signal detection. Moreover, waveguide PDs serve as pivotal components in photonic integrated circuits (PICs). Their integration within these circuits further underscores their importance, as PICs are the bedrock of modern optoelectronic systems, amalgamating multiple optical functions on a single chip, which enhances performance while minimizing size and cost.
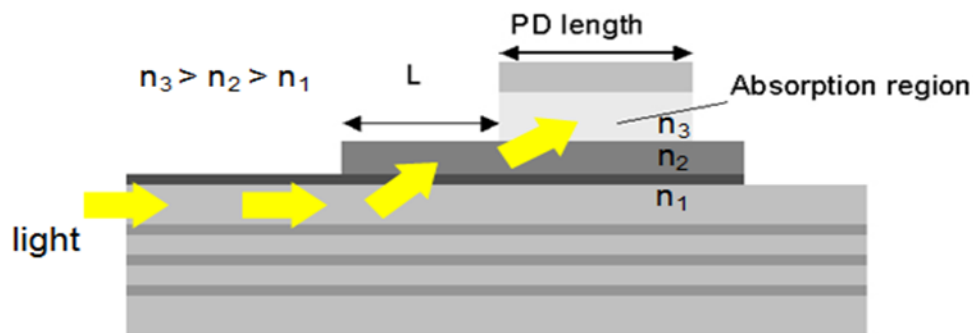
Figure 11. Evanescently-coupled Waveguide PD [19]

However, it is important to consider the specific design features of waveguide PDs. Many waveguide PDs are either butt- or evanescently coupled in the figure 11, which influences their responsivity characteristics. The responsivity of such PDs is primarily determined by the length of the absorber layer within the waveguide. While this configuration can enhance responsivity, it may also introduce potential drawbacks.

In high-responsivity PDs, the scaling of responsivity with the absorber layer length can negatively impact both the bandwidth and dark current. The increased length of the absorber layer can lead to a decrease in the device's bandwidth, limiting its ability to handle high-frequency signals efficiently. Additionally, the longer absorption length may result in higher dark current due to the larger absorber volume, leading to increased noise levels and reduced signal-to-noise ratio.

In conclusion, waveguide photodiodes offer promising solutions to the bandwidth-efficiency trade-off in traditional PDs, enabling high-speed and high-efficiency signal detection. While their responsivity benefits from the length of the absorber layer, careful design considerations are essential to address potential challenges related to bandwidth and dark current, paving the way for improved photodiode technology in the future.

1.6 Segmented waveguide photodetector

The concept of segmented photodiodes draws inspiration from Professor Andreas' PhD thesis [19]. Professor Andreas discussed the design concept of segmented TWPD (S-TWPD) shown in the figure 12, in contrast to the parallel-fed traveling-wave photodiode (TWPD), the photodiodes in the segmented TWPD are arranged in series on top of a single optical waveguide. Each photodiode absorbs only a fraction of the light propagating in the waveguide, and the transmitted portion couples to the next detector region, and so on. The ultimate goal is to achieve complete light absorption at the end of the device by employing a sufficiently large number of photodiodes, leading to enhanced responsivity and linear photocurrent compared to a single photodiode. Therefore, it is crucial to design each individual PD with low radiation loss at its rear side to optimize the overall performance of the segmented PD device.
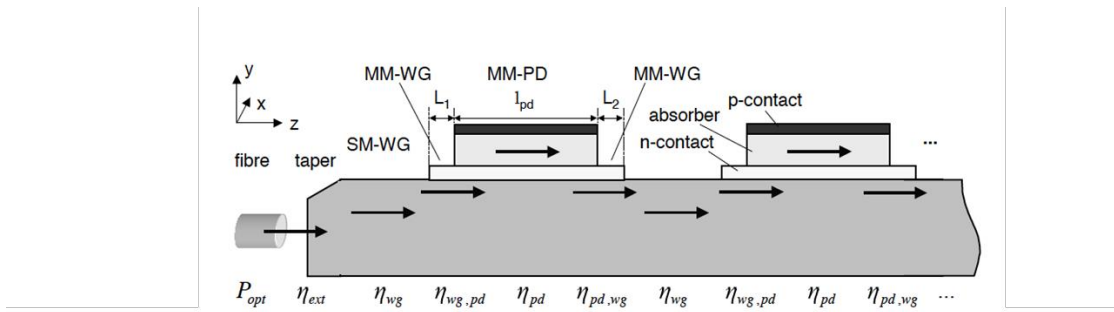
$$ R = R_{ideal} \cdot \eta_{ext} \left[\sum_{i=1}^{n} \eta_{wg}^{i} \cdot \eta_{wg,pd}^{i} \cdot \eta_{pd}^{i-1} \cdot \eta_{pd,wg}^{i-1} \right] \cdot \left[1 - exp\left(-\int_{0}^{L_{pd}} \alpha_{eff}(z)\, dz \right) \right] $$

Figure 12. Schematic view of two sections of a serial-fed TWPD with spot-size converter. The corresponding coupling efficiencies are η [19]

In this study, a method for photon number resolution using segmented PDs with low dark currents is proposed. The setup involves placing segmented PDs along a long waveguide, where each PD sequentially captures few photons at a time. This arrangement allows photons not absorbed in the first PD to couple back into the waveguide and be subsequently absorbed in one of the following detectors. One significant advantage of this configuration is that the non-ideal quantum efficiency of the PDs does not result in photon loss, unlike butt-coupled PNR detectors, where temporally or spatially split photons impinge on PDs at the end of their path. Thus, the linear array of segmented PDs functions as a long detector divided into multiple short detectors, each with an individual read-out capability. We envision that such a segmented photodetector could be feasible in large-scale integrated photonic platforms using either monolithic or heterogeneous integration of PDs on low-loss waveguides.

To understand the principle of segmented waveguide photodetectors (SWPDs) coupling, a simplified model is used as the figure 13, assuming that the SPAD length is equal to the period of the mode beat between the main waveguide and the SPAD. This model is sufficient for the analysis of the photon number-

resolving (PNR) behavior. The quantum efficiency of the SPAD, denoted as $\alpha2$, accounts for both the coupling efficiency and intrinsic absorption, resulting in a field transmissivity of $1-\alpha2$. To minimize the probability of any SPAD detecting more than one photon during the same detection window, it is desirable for $\alpha2$ not to be too large.
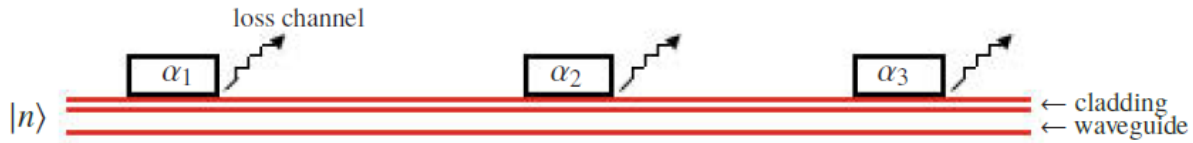
Figure 13. Segmented detector. Guided optics are used to detect photons alongside propagation by PDs. The design goal is to keep all undetected photons in the waveguide, for further detection [2]

In summary, SWPDs can offer high quantum efficiency and photon number resolution, making them promising candidates for various applications, including quantum measurements and high-speed optical communications. The integration of SWPDs with other devices further enhances their functionality, making them valuable tools in modern photonics research. In addition to their use in quantum measurements, the design of SWPDs has broad applications in various fields, such as high-speed optical communications or sensing. By integrating SWPDs with other devices, such as lock-in amplifiers and phase-shift interferometers, additional functionalities can be achieved.

Chapter 2. Device Principle and Theory

2.1 Operating physics principle of segmented waveguide photodetector

This study presents a novel design for a segmented waveguide photodetector, drawing inspiration from the Uni-Traveling-Carrier Photodiode (UTC-PD) concept. By incorporating key features of the UTC-PD, such as the neutral absorber and electron collection layer, the segmented waveguide photodetector achieves improved light absorption and carrier collection efficiency. The design involves two waveguides, with waveguide 2 optimized for efficient photon absorption as the neutral absorber, and waveguide 1 acting as the electron collection layer or collector, facilitating efficient carrier collection and minimizing recombination losses.

The operating principle of segmented waveguide photodetector is based on the waveguide-coupled absorption of incident photons in the segmented detector structure. I used p-i-n PD in my work for simplicity, but results can be applied to APDs and SPADs. As shown in the figure 14, the detector consists of multiple segments of p-i-n diodes separated by waveguides. The waveguides serve as channels for light propagation and guide the photons to the absorption regions of the detector. The p-i-n diodes are responsible for absorbing the photons and generating electron-hole pairs, which are collected and detected as photocurrent.
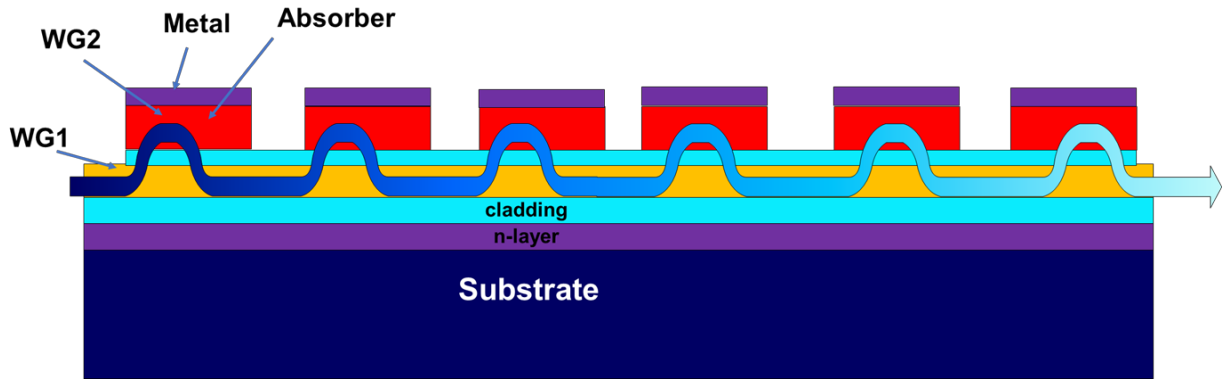
Figure 14. Principle of Light propagating in the segmented waveguide photodetector

The key feature of segmented waveguide photodetector is the use of multiple absorption regions separated by passive waveguides. This allows for the absorption of a single photon in one segment without the loss of subsequent photons. The segmented structure also provides a means for spatial and spectral filtering, enabling the detection of specific wavelengths and polarization states.

The quantum efficiency of the detector is a critical parameter for its performance in photon counting applications. In segmented waveguide photodetector, the quantum efficiency is determined by the absorption probability of the photons in the p-i-n diodes. The absorption probability is affected by the absorption coefficient of the diode material, the thickness of the absorption region, and the overlap of the optical mode with the absorption region. In fact, in the segmented detector the absorption in each PD is very small.

In addition to quantum efficiency, other important parameters for segmented waveguide photodetector include responsivity, dark current, and bandwidth. Responsivity is a measure of the detector's sensitivity to incident photons and is proportional to the generated photocurrent per incident photon. Dark current is the current that flows through the detector in the absence of light and can limit the sensitivity and dynamic range of the detector. Bandwidth is a measure of the frequency range over which the detector can operate and is determined by the capacitance and resistance of the detector.

In the following sections, I will discuss the device physics and design considerations for segmented waveguide photodetector in more detail.

2.2 Directional coupler design

The proposed photodetector utilizes a directional coupler configuration to enhance the light coupling efficiency into the segmented waveguide structure. In this study, I discuss the principles behind the design of directional couplers, focusing on the interaction between the coupled waveguides and the efficient transmission of optical power. The advantages of this design are highlighted, emphasizing its potential to improve light coupling efficiency and overall device performance.

Directional couplers are a type of multiple-waveguide couplers that facilitate codirectional coupling. These couplers find applications in various optical devices, such as power splitters, optical switches, wavelength filters, and polarization selectors. I specifically consider two-channel directional couplers composed of two parallel waveguides.
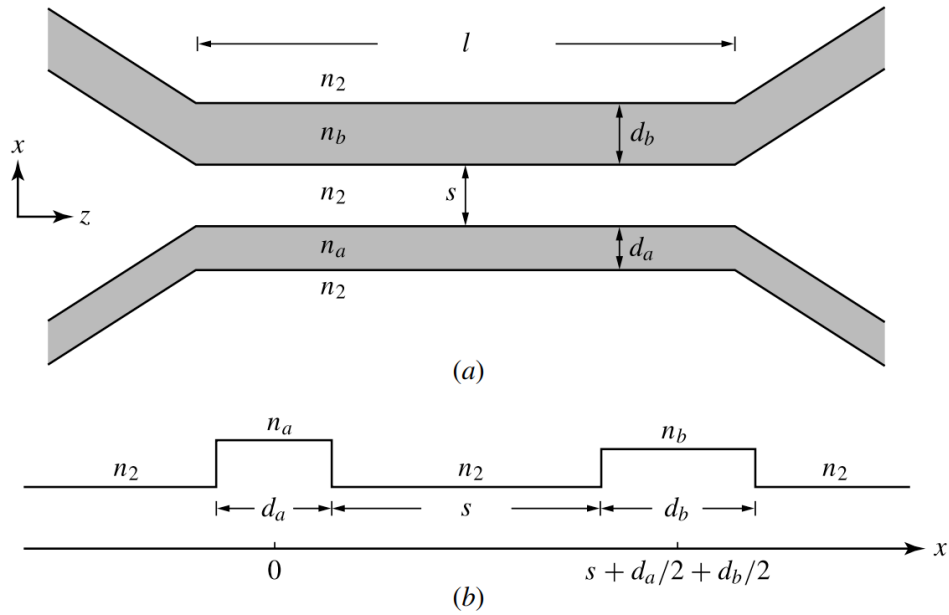
Figure 15. Directional coupler [20]

As shown in figure 15 above, the two waveguides have widths d_a and d_b and guiding layer refractive indices n_a and n_b, respectively. They are separated by a distance s between the two near edges of the guiding layers. The index of refraction of the substrate is n_2. When $n_a = n_b = n_1$ and $d_a = d_b = d$, the coupler is symmetric. Otherwise, it is asymmetric. The coupling length is l, the gap of the two waveguides is s.

In symmetric couplers, two waveguides are closely spaced, and their modes evanescently couple with each other. As a result, the power is transmitted between the waveguides due to the overlapping of modes in the central region. The maximum power transmission occurs when the coupler is symmetric.
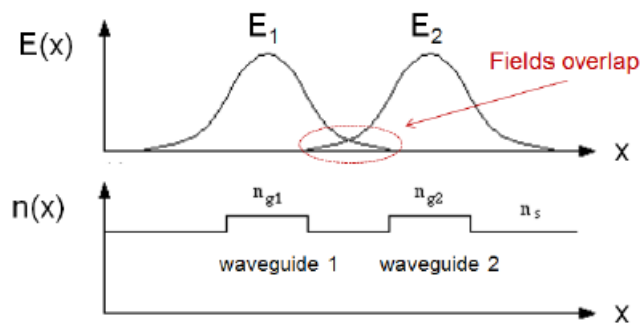
Figure 16. Cross section in coupling region [21]

In this configuration as the figure 16 shows, the coupler can act as a beam splitter, dividing the input power equally between the two output ports. Additionally, there is a 90-degree phase shift for the power transmitted to the cross port compared to the through port. This phase shift is a characteristic feature of symmetric couplers and plays a crucial role in various applications, such as interferometry and directional couplers for optical switches and power splitters.

14

2.3 Structure of segmented waveguide photodiodes

The fundamental operation principle of SWPDs lies in their ability to efficiently couple light into the segmented waveguide structure. The segmentation allows for sequential absorption of photons in each segment, resulting in improved total quantum efficiency. The coupling efficiency is further optimized by employing directional coupler configurations, where the interaction between the waveguides facilitates efficient light coupling into the segmented waveguide regions.

Furthermore, the structure and design of SWPDs ensure that each segment absorbs only a fraction of the incident light, allowing the remaining light to couple to the next detector region. This sequential absorption process ensures that the light is efficiently absorbed by the end of the device, resulting in improved responsivity and linear photocurrent.

In this chapter, I will delve deeper into the detailed structure, operational principles, and specific advantages of SWPDs, providing a comprehensive understanding of their potential and significance in modern photonic technologies.

SWPDs consist of a waveguide structure with a segmented p-i-n junction, as shown in the figure 17. The waveguide structure is typically made of III-V semiconductor materials such as InP or GaAs. The segmented p-i-n junction is created by selectively doping the semiconductor layers, which enables the separation of the photogenerated carriers and the efficient collection of the photocurrent.

The waveguide structure of SWPDs is designed to provide efficient optical coupling between the input light and the segmented p-i-n junction. The input light is coupled into the waveguide through a coupling region, which is designed to match the mode of the input light to the mode of the waveguide. The light then propagates along the waveguide and is absorbed by the segmented p-i-n junction. The photocurrent generated in the segmented p-i-n junction is collected by the metal contacts at the edges of the device.

(a)   (b)
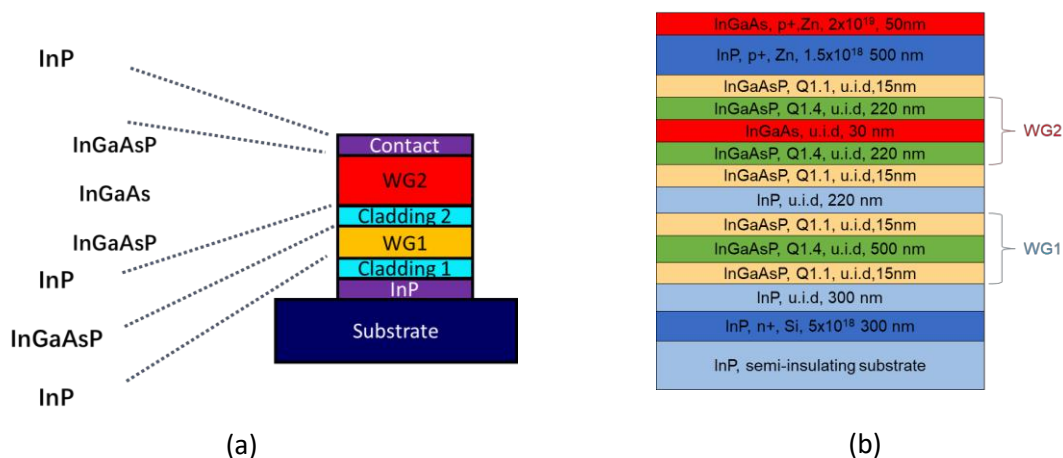
Figure 17. (a) Cross-section of waveguide photodiode; (b) Epitaxial layer structure for segmented waveguide photodetector [1]

Therefore, I can choose specific materials, doping levels, refractive indices, and thicknesses for each layer that I used in the simulations, as shown in the table below:

Table 1. The specific materials and parameters I used in the simulation

Material of layer(with doping)	refractive indices n	Thickness d (nm)
InGaAs, p+,Zn, 2×10^{19},	3.56	50
InP, p+, Zn, 1.5×10^{18}	3.1649	500
InGaAsP, Q1.1, u.i.d,	3.24	15
InGaAsP, Q1.4, u.i.d,	3.42	220
InGaAs, u.i.d,	3.56+0.147i	30
InGaAsP, Q1.4, u.i.d,	3.42	220
InGaAsP, Q1.1, u.i.d,	3.24	15
InP, u.i.d,	3.1649	220
InGaAsP, Q1.1, u.i.d,	3.24	15
InGaAsP, Q1.4, u.i.d,	3.42	500
InGaAsP, Q1.1, u.i.d,	3.24	15
InP, u.i.d,	3.1649	300
InP, n+, Si, 5×10^{18}	3.1649	300
InP, semi-insulating substrate	3.1649	hundreds of microns
Total Length except substrate		154.6875

2.4 Supermode in the coupled waveguide

In optical waveguide systems, when two waveguides are brought close to each other, their individual modes begin to interact, giving rise to a unique phenomenon known as the supermode. The supermode is distinct from the fundamental mode found in the individual waveguide and emerge due to the coupling between adjacent waveguides.

The supermode is the superposition of two modes, which is higher-order mode specific to coupled waveguides, meaning they don't exist within the standalone waveguide's fundamental modes. Their genesis is rooted in the interaction between two closely placed waveguides, especially when they possess different refractive indices. The close proximity of the waveguides allows their optical fields to overlap, leading to a combined mode structure that's different from the individual waveguides.

In simpler terms, while each waveguide typically supports its own set of modes, the act of coupling or bringing two waveguides close together leads to the creation of the supermode. These new modes span both waveguides and are a direct result of the interaction between the modes of the individual waveguides.

In the waveguide design, achieving similar effective refractive indices between two waveguides is desirable to facilitate efficient coupling and transmission effects, leading to improved coupling efficiency, light transmission, and reduced energy loss and reflection.
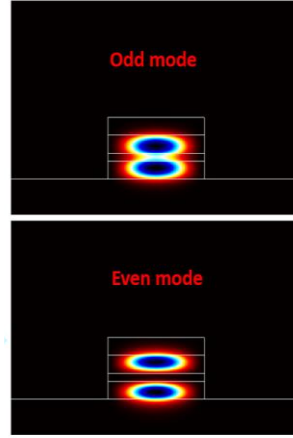
In the context of waveguide design, achieving similar effective refractive indices between two waveguides is of paramount importance, as it facilitates efficient coupling and transmission effects, leading to enhanced coupling efficiency, improved light transmission, and reduced energy loss and reflection. The process of light coupling into and out of a photodetector can be treated as a co-directional coupler problem, as illustrated in the figure 15(a). To ensure seamless coupling, the fundamental goal is to achieve phase match, which involves aligning the propagation constants of the modes in waveguides WG1 and WG2.

In the figure 18, the intensity distribution of the odd (anti- symmetric) mode and even (symmetric) mode in the waveguide cross-section is shown, thus:

Supermode = Odd (anti- symmetric) mode + Even (symmetric) mode

Following the well-established theory of mode coupling , the field distribution $\Phi_1(z)$ in WG1 and $\Phi_2(z)$ in WG2 can be represented by a linear combination of the even mode field ϕ_e and the odd mode field ϕ_o:

$$\Phi_1(z) = a_1\phi_e\exp\left(-i\beta_e z\right) + a_2\phi_o\exp\left(-i\beta_o z\right)$$
$$\Phi_2(z) = a_3\phi_e\exp\left(-i\beta_e z\right) + a_4\phi_o\exp\left(-i\beta_o z\right)$$

Here, β_e and β_o denote the corresponding propagation constants of the even and odd modes, respectively, and a_1, a_2, a_3, and a_4 are the coupling coefficients. Upon launching light into WG1 at $z = 0$, the coupling condition $\Phi_2(0) = a_3\phi_e + a_4\phi_o = 0$ ensures efficient power transmitted from WG1 to WG2. To minimize radiation loss, it is necessary for light to fully couple back from WG2 into WG1 at the rear facet of the PD, which is achieved when $\Phi_2\left(l_{pd}\right) = 0$.

Combining these conditions with the initial conditions leads to the phase match requirement for the odd and even modes:

$$\exp\left(-i\Delta\beta l_{pd}\right) = 1$$

Here, $\Delta\beta$ represents the difference between the propagation constants of the even and odd modes, defined as $\Delta\beta = \beta_e - \beta_o$. To express $\Delta\beta$ as a complex number, I define $\Delta\beta = \Delta\beta_r + i\Delta\beta_i$, where $\Delta\beta_r$ and $\Delta\beta_i$ are the real and imaginary parts of $\Delta\beta$, respectively. Consequently, the phase match condition can be written as:

$$\exp\left(\Delta\beta_i l_{pd}\right)\exp\left(-i\Delta\beta_r l_{pd}\right) = 1$$

To satisfy this condition, it is imperative to set $\Delta\beta_i = 0$, indicating that the propagation constants of the odd and even modes must possess identical imaginary parts. In other words, only when both modes experience equal attenuation rates can a complete transmission of optical power between WG1 and WG2 be achieved.

Furthermore, Euler's identity represents the equality $e^{i\pi} + 1 = 0$. By combining this identity with the phase match condition $\exp\left(-i\Delta\beta_r l_{pd}\right) = 1$, I can deduce that the photodetector length l_{pd} must be a multiple of the beat length l, defined as $l = \frac{2\pi}{\Delta\beta_r}$.

This criterion guarantees that the interference pattern between the even and odd modes periodically repeats over a distance l, resulting in efficient and periodic coupling of light between the two waveguides. The periodicity enabled by the beat length ensures that light experiences constructive and destructive interference, leading to the complete transmission of optical power between the waveguides. As a consequence, this phenomenon plays a critical role in optimizing the design and performance of waveguides, thereby enhancing their overall functionality in optical systems and applications.

Chapter 3. Principle of FIMMWAVE Software

The FIMMPROP software is a tool designed to model the propagation of light in various periodic structures, including gratings, Bragg reflectors, polarization rotators, surface emitters, and mode converters. Its capabilities extend to handling diverse geometries, such as planar waveguides, optical fibers, and more complex structures.

FIMMWAVE serves as a waveguide mode solver, determining the eigenmodes, which are solutions of Maxwell's Equations in z-invariant refractive index profiles of the form Φ

$$\Phi(x, y, z) = \psi_m(x, y) \cdot e^{i\beta z}$$

Here, β represents the propagation constant of the mode. An analogy can be drawn between these modes and the eigenmodes of a violin string, where y(x) denotes an arbitrary eigenmode.

The concept of the effective index (n_{eff}) is introduced as the ratio of the propagation constant (β) to the wavenumber in free space (k_0), expressed as

$$n_{eff} = \frac{\beta}{k_0}$$

$$k_0 = 2\pi/\lambda$$

where λ represents the wavelength.

Additionally, the confinement factor (Γ) is defined as it relates to the mode loss (α_{mode}) through the equation $\alpha_{mode} = \Gamma_j \cdot \alpha_{material,j}$.
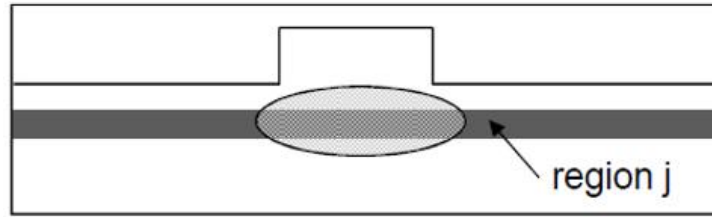
Furthermore, the orthogonality of modes is highlighted, with the integral of the product of two modes

$$\int \phi_i(x,y)\phi_k(x,y)dxdy \quad = 1, \text{if } i = k$$
$$= 0, \text{if } i \neq k$$

In fact, I inspect only the TE mode to carry out the simulation work, with a wavelength of 1.55μm.

3.1 Boundary condition

FIMMWAVE offers a comprehensive range of boundary conditions to accommodate various simulation scenarios. These conditions include perfect electric wall and perfect magnetic wall constraints, impedance boundary conditions (applicable anywhere between the perfect electric wall and the perfect magnetic wall), transparent boundary conditions, periodic boundary conditions, and Perfectly Matching Layers (PMLs). When light couples to radiation modes and interacts with the simulation boundaries, it becomes necessary to incorporate PMLs (Perfectly Matched Layers) or ABC boundaries (Absorbing Boundary Conditions) to prevent unwanted reflections [23]. When using PMLs, maintaining a consistent cross-sectional size and retaining identical solver settings throughout the structure is essential for achieving more accurate results.

In my simulations, because I used FIMMWAVE software for designing structures similar to directional couplers, I chose Perfectly Matching Layers (PMLs) as the preferred boundary conditions. This decision was influenced by the observed attenuation at the boundaries of my structure, and PMLs proved highly effective in mitigating this attenuation by absorbing or minimizing reflections along the edges of the simulation domain.

3.2 Solver mode

FIMMWAVE software provides support for various mode solvers, including the FMM Solver (based on the film mode matching method), FDM Solver (based on the finite difference mode method), and the FEM Solver (based on the finite-element method) [24].

In my case, I opted for the FDM Solver This solver relies on advanced finite-difference algorithms and excels in simulating metallic or absorbing structures. It offers precise modeling capabilities for complex waveguide structures, including those with high-step refractive index profiles, slanting or curved interfaces,

and gradient profiles. Considering the nature of my structure, particularly the potential presence of absorption characteristics, the FDM Solver emerged as the most suitable choice.

When it comes to solver modes, a thorough evaluation of the structural characteristics under analysis is essential. As depicted in the figure 20, a complex solver is generally recommended when the structure exhibits attenuation at its boundaries, often due to the inclusion of Perfectly Matching Layers (PMLs) or material absorption. Complex solvers excel in accurately depicting the interaction of light with absorptive or lossy materials.
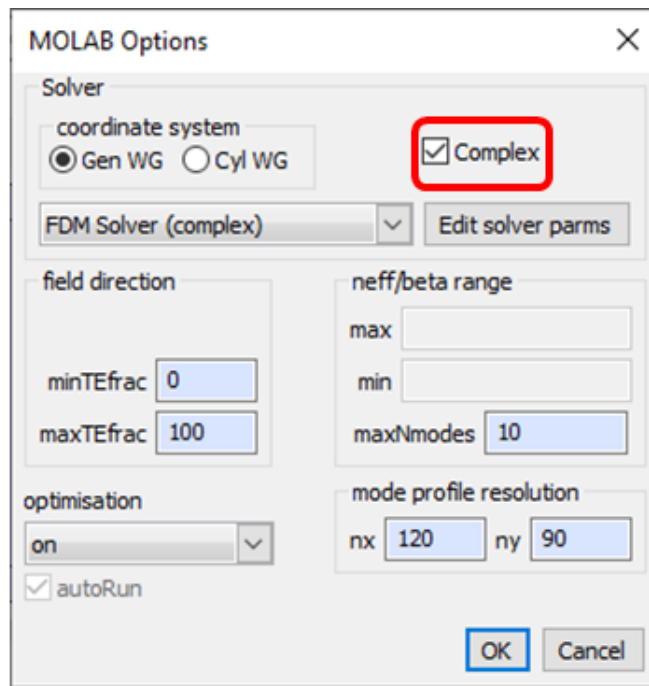
Figure 20. Settings for the complex solver

Nevertheless, it is vital to acknowledge that the use of a complex solver can significantly extend computation time, potentially by a factor of up to four or more. Consequently, careful consideration is necessary when introducing Perfectly Matching Layers (PMLs) into the simulation. The inclusion of PMLs can introduce complexity into the optimization process, as it requires optimizing not only other parameters but also the width of the PMLs themselves. This decision should be made thoughtfully, weighing the necessity of accurately representing the specific structural characteristics against the available computational resources for the simulations.

3.3 EME

When modeling gratings in FIMMPROP, one has the choice between two computational methods: EigenMode Expansion (EME) and Rigorous Coupled Mode Theory (RCMT), an innovative technique developed by Photon Design. These two methods complement each other and deliver precise and efficient modeling for different grating geometries.

I used EME for modeling high-order gratings like co-directional couplers and surface grating couplers. The reason for choosing EME is that it represents a robust and rigorous approach within FIMMPROP for modeling optical propagation. EME offers several advantages:

- Bi-directional simulations: EME allows for conducting bi-directional simulations of light propagation, which is crucial for accurately modeling complex structures. This capability is particularly useful when analyzing structures with variations along the propagation direction.

- Precision: EME provides a high level of precision in modeling optical propagation. It can surpass the accuracy achieved by other techniques such as Finite-Difference Time-Domain (FDTD), Beam Propagation Method (BPM), or Finite Element Method (FEM).

- Mode matching principle: EME is based on the fundamental principle of mode matching, which makes it suitable for analyzing structures that may not exhibit invariance in the z-direction. This is important for handling non-uniform and complex structures.

The concept behind EME has been well-established in photonics for some time. At its core, it starts with defining the "mode" or "eigenmode" of a waveguide. In cases where the optical refractive index remains constant along the z-direction, I discover solutions to Maxwell's Equations in the form of:

$$\vec{E}(x, y, z) = \vec{e}_m(x, y) \cdot e^{i\beta_m z}$$

(assuming a single wavelength and time dependence in the form of $\exp(i\omega t)$). Mathematically, $\vec{e}_m(x, y)$ and β_m represent the eigenfunction and eigenvalue of the solution. Consequently, modes exhibit a straightforward harmonic z-dependence, which is a crucial factor enabling EME to efficiently solve extended, slowly varying structures.

In a typical waveguide, there exist guided modes (propagating without loss along the waveguide) alongside an infinite number of radiation modes (carrying optical power away from the waveguide). Together, these guided and radiation modes form a complete basis set. In other words, any solution of Maxwell's Equations within the waveguide region can be expressed as a superposition of forward and backward propagating modes (as shown in Equation 2):

$$\vec{E}(x, y, z) = \sum_{k=1}^{M} \left(a_k e^{i\beta_k z} + b_k e^{-i\beta_k z} \right) \vec{E}_k(x, y)$$

This equation demonstrates its bi-directional nature and represents an exact solution of Maxwell's Equations in a linear medium. However, up to this point, EME has been primarily applicable to z-invariant structures.

One of the distinguishing strengths of EME lies in its ability to model discontinuities, such as the interface between two waveguides. By imposing Maxwell's Equations continuity conditions for the fields, relationships among the coefficients of various modes can be established. These relationships are succinctly expressed using a scattering matrix (S_J) for the interface.
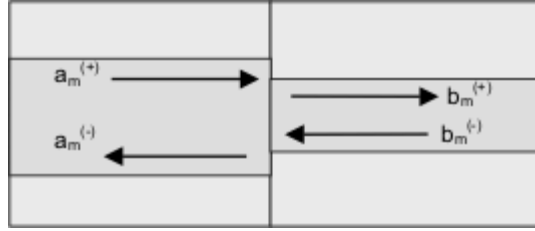
The figure 21 illustrates mode coefficients at such an interface, where Maxwell's Equations continuity conditions allow the derivation of a relationship in the form of:

$$\begin{pmatrix} \vec{a}^- \\ \vec{b}^+ \end{pmatrix} = S_J \begin{pmatrix} \vec{a}^+ \\ \vec{b}^- \end{pmatrix}$$

Here, S_J represents a scattering matrix for the interface, indicating how the incident fields relate to the fields propagating away from the interface.

To extend this expansion to any component, I can write a scattering matrix (S_WG) for a straight section, which simplifies as follows:

$$S_W G = \begin{pmatrix} e^{i\beta_1 z} & 0 & 0 & \cdots \\ 0 & e^{i\beta_2 z} & 0 & \cdots \\ 0 & 0 & e^{i\beta_3 z} & \cdots \\ \vdots & \vdots & \vdots & \ddots \end{pmatrix}$$

This matrix is straightforward to compute once the eigenmodes have been determined.

Consider now a common photonics component—the MMI coupler—as depicted in the figure 22. This component is among the many that can be effectively analyzed using EME techniques.
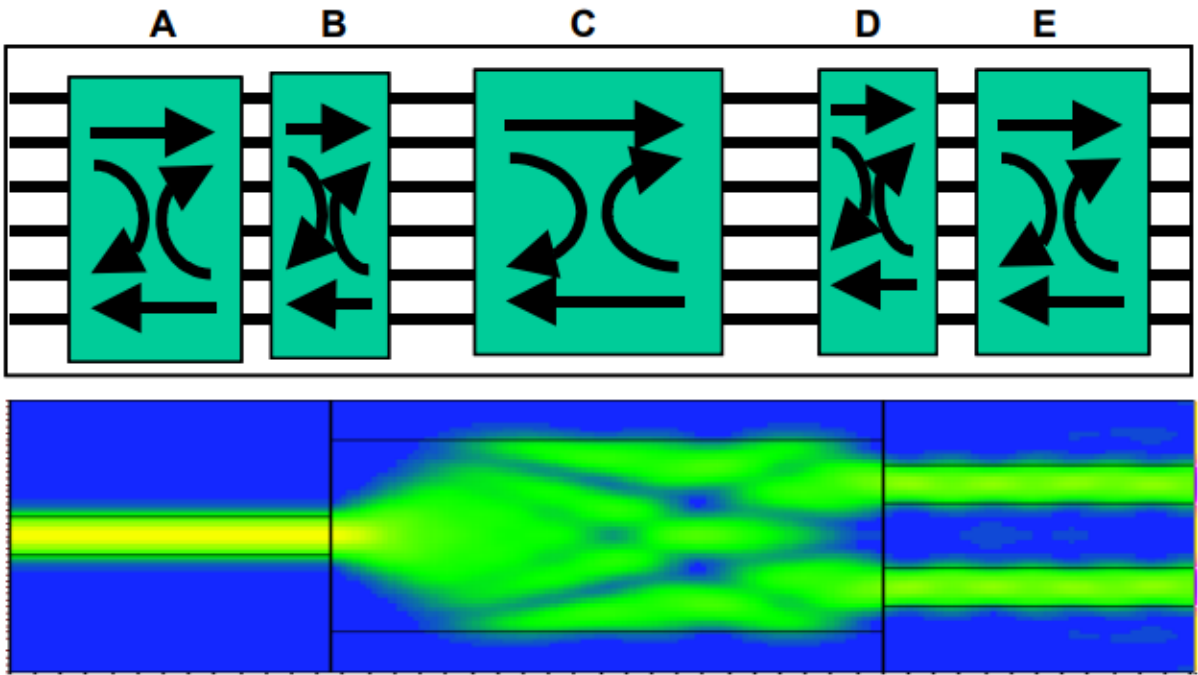
The utilization of EME enables the expansion of optical fields in terms of a comprehensive mode set. This expansion facilitates the computation of scattering matrices for various components. As an example, the scattering matrix for a straight section becomes straightforward to compute once the eigenmodes have been determined. The method's capacity to handle structural discontinuities and non-z-invariant configurations sets it apart from alternative simulation techniques, enabling precise and efficient analysis of a diverse array of photonic components and devices.

3.4 Scattering matrix

The periodic structures, consisting of repeated identical periods, can be efficiently computed using EME due to a key advantage: the S-matrix of one period remains identical to that of every other period. Consequently, the computational effort required for periodic structures is nearly as swift as that for a straight waveguide. This efficiency makes EME an excellent choice for modeling such structures.

I can calculate the scattering matrix of an entire FIMMPROP Device or FIMMPROP Layout by clicking on the FIMMPROP menu. The Scattering Matrix of a given element can also be displayed by right-clicking on this element and selecting Niew Element S matrix.

In FIMMPROP, the overall Scattering Matrix has the form: $\{T', T, R^l, R^r\}$, and is defined by giving the coefficients of the output field C^b, C^f in terms of those of the input field C^f, C^b :

$$\mathbf{C}^{lf} = \mathbf{T}^l \mathbf{C}^{lf} + \mathbf{R}^r \mathbf{C}^{rb}; \ \mathbf{C}^{lb} = \mathbf{R}^l \mathbf{C}^{lf} + \mathbf{T}^r \mathbf{C}^{rb}$$

Where:

- $\{\mathbf{C}^{lf}, \mathbf{C}^{b}\}$ are the mode amplitude coefficients at the beginning of the leftmost Section.

- $\{C^{rb}, C^{ff}\}$ are the mode amplitude coefficients at the end of the rightmost Section.

Hence the components of the overall Scattering Matrix are:

- T^1 = Transmitted from Left side.
- T^r = Transmitted from Right side.
- R^1 = Reflected from Left side.
- R^r = Reflected from Right side.

The power, amplitude and phase correspond to the mode coefficients. These mode coefficients C can be expressed as $C = ampl \cdot e^{i \cdot phase} = real + j \cdot imag$, with $power = |ampl|^2$.

Chapter 4. Design, Simulation, and Optimization of Segmented Waveguide Photodetector

4.1 Design of segmented waveguide photodetector

In the software FIMMWAVE, I set up the simulation by defining the geometries of the waveguide and photodiode, as well as their material properties and the light source.

Building upon the prior work of Qianhuan Yu, I first re-simulated the initial device design. As shown in the figure 23, the structure of the device, from bottom to top, features WG1 and WG2 as the passive and active waveguides, respectively. Within the active WG, the absorber layer is made of InGaAs.
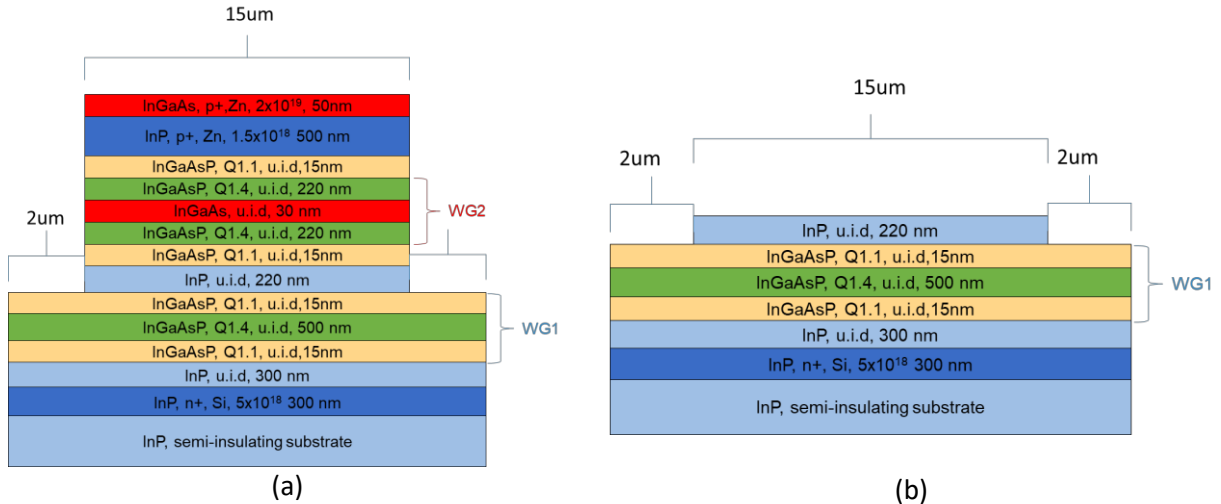
Figure 23. Materials and structures of each layer of (a)PD device and (b) Passive WG1

From the actual FIMMWAVE simulation, I observed both the Cross Section - XY and the Planar Section - YZ in the provided figure 24. It's evident that the passive waveguide corresponds to the structure of the lower waveguide, while the central region represents the PD structure. This figure elucidates the architecture of each waveguide and the PD, facilitating the identification of parameters such as layer size and material composition across the entire three-dimensional structure.
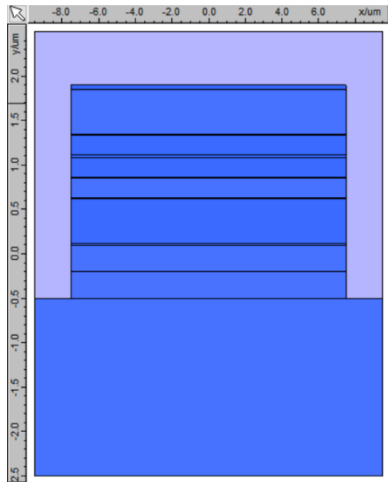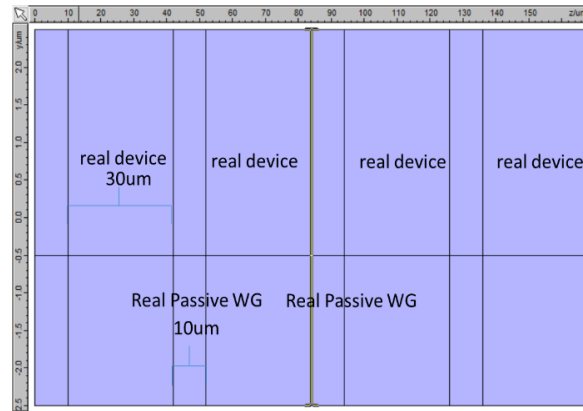
Cross Section - XY   Planar Section -   YZ

Figure 24. XY and Planar Section- YZ from the figure in FIMMWAVE

While I have the option to transform the right-side illustration into an XZ orientation, I opt for the YZ direction since the field path I've designed is along the YZ axis. Moreover, by selecting any specific section, I can gain a detailed view of the XY structure on the left. This offers a clear perspective of how passive and active waveguides are alternately arranged.

In the computational framework of FIMMWAVE, the accurate determination of the absorption coefficient α(cm^{-1}) and the complex refractive index $m(\lambda)$ is critical. FIMMWAVE offers both real and complex solvers. The real solver computes mode loss by performing an overlap integral with the material's absorption coefficient profile, focusing solely on scattering effects. Conversely, the complex solver generates a profile for $m(\lambda)$, considering both scattering and absorption.

The complex refractive index is expressed as $m(\lambda) = m_r(\lambda) + im_i(\lambda)$, where λ is the freespace wavelength in μm, m_r is the real part, and m_i is the imaginary part. The real part m_r signifies the ratio of the free-space speed of light to the phase speed of an electromagnetic wave in the medium. The imaginary part m_i is intrinsically related to the absorption coefficient, with $\alpha = 4\pi m_i/\lambda$.

I reviewed InGaAs at a wavelength of 1550 nm. As shown in the figure 25, the absorption coefficient typically ranges from 6000 to 8000 cm^{-1}[26], contingent upon the doping level. In this study, an absorption coefficient of 7000 cm^{-1} was selected as representative for InGaAs.
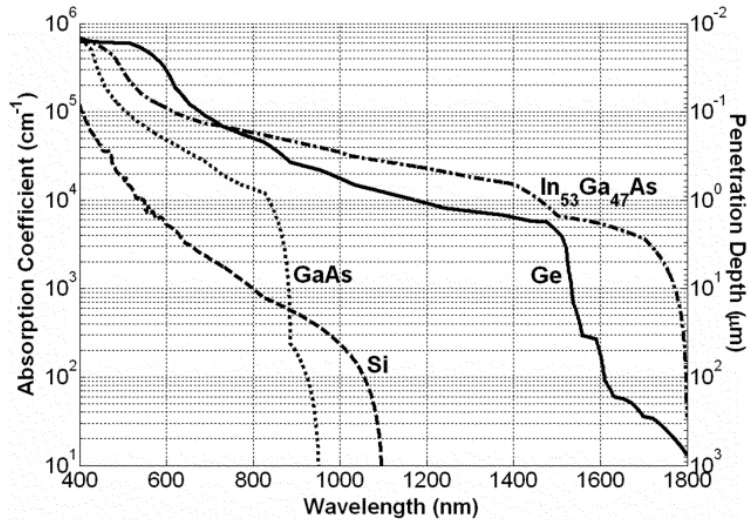
Figure 25. Absorption coefficients for various semiconductors [26]

So I can design a single cycle as the figure 26 shows. It can make sense to define the following: WG1, WG2, PD length and active/passive sections, α, β, γ, and cladding etching depth.
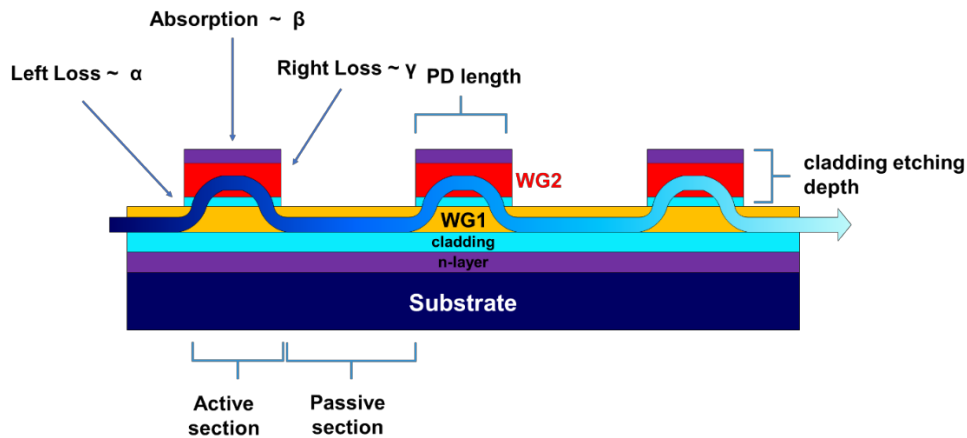
Figure 26. Principle of α, β, and γ and other geometry

Left Loss (α): This factor represents the loss of photons on the photodetector's left side. Such losses can be attributed to various phenomena, including radiation losses stemming from reflection and scattering at the front surface of the PD. Specifically, it accounts for photons that fail to transmit from WG1 to WG2, predominantly originating from radiation losses between these waveguides.

Absorption (β): This factor represents the loss due to absorption of the photodiode, indicating the percentage of incident photons that are absorbed within the absorber layer. It considers the ability of the material to capture photons and convert them into electrical signals.

Right Loss (γ): This factor represents the loss of photons on the right side of the photodetector at the end surface, including any further radiation losses that occur after passing through the absorber layer. It accounts for the photons that do not reach the WG1 from WG2.

The remaining power ratio for a system of segments PDs arranged in series is:

$$\text{Remaining power ratio} \leq \text{setting ratio}$$

The remaining power ratio represents the remaining power ratio over the total injecting power of the segmented PD, considering the combined effects of all loss. The setting ratio is the minimum power ratio that is continuously effective for a single cycle, and it is guaranteed to be useless in the next cycle, generally one thousandth.

It is important to note that this calculation assumes independence between the individual PDs and that the loss factors (α, β, and γ) remain constant across all PDs. Additionally, it's essential to validate this mathematical model through experimental data and consider any variations or non-idealities that may arise in practical implementations.

The optimization goals of the simulation encompass a multifaceted approach aimed at achieving enhanced performance. Central to these objectives is the imperative to diminish both α and γ losses, strategically minimizing any inefficiencies in the system. Simultaneously, a pivotal focus lies in the continuous improvement of the total quantum efficiency, ensuring an optimal utilization of photons. Additionally, the simulation aims to maximize the number of PDs, thereby fulfill the requirement of the single-photon counting. This comprehensive strategy underscores the commitment to refining and fine-tuning various parameters to attain an optimal and efficient simulation outcome.

In the simulation framework used in FIMMWAVE, several potential loss mechanisms are not considered, including waveguide losses (due to material loss) between segment photodiodes, and loss in metal contacts. Due to FIMMWAVE's limitations in directly parameterizing waveguide losses, these additional losses originating from WG1 can be integrated into our material computations. It is worth noting that assuming low-loss waveguides, such as a low-loss Si_3N_4 waveguide (0.1 dB/cm) [27] or an InGaAsP waveguide (0.4 dB/cm) [28] and incorporating these values into the material properties can provide a more accurate representation of waveguide losses in simulations. However, compared to radiation losses, waveguide losses are sufficiently negligible, justifying their exclusion from the optimization processes conducted in this thesis.

Understanding and optimizing these loss factors is critically important for enhancing the performance and efficiency of photodetectors. Further analyses and experimental investigations are warranted to quantify these loss mechanisms comprehensively and to explore strategies for loss minimization and quantum efficiency improvement in photodetectors.

4.2 Analysis of a single PD cycle

Because Multiple Segmented Photodetectors (PDs) have a periodic structure, I can analyze the performance of a single PD and extend the results to the entire system. By analyzing a single segmented PD, I can obtain information about its radiation loss, quantum efficiency, and other performance metrics.

These performance indicators are crucial for evaluating the overall performance and optimizing the design of the entire multiple segmented photodetector system.

In my initial research, building upon the foundational work of Qianhuan Yu, I conducted a re-simulation to delve into the interrelation between the thickness of the PD absorber layer, the field distribution, scattering matrix and the propagation constants. This was pursued with the dual intent of replicating and further enhancing the original findings. The field distribution is pivotal, acting as a metric to ascertain if the modal propagation conforms to the tenets of the directional coupler, a cornerstone in the design blueprint of segmented PDs. Conversely, the propagation constant offers valuable perspectives into the effectiveness of the photonic coupling. Notably, as the propagation constant embodies both its real and imaginary facets, it becomes essential to judiciously weigh their synchronous match in the analysis.

In the 2018 OE paper of Qianhuan Yu [1], to ensure that only the fundamental mode propagates in the passive waveguide regions, he designed an 800 μm long tapered input waveguide. The waveguide width is 4 μm at the input (facet) and matches the PD width at its opposite end. His simulations revealed that fundamental mode propagation can be maintained throughout the entire segmented waveguide PD.

I firstly have re-simulate previous result in the figure 27(a), when the device which the PD width is 20 μm, PD length is 32 μm and absorber thickness is 30 nm for a single cycle, my result in the figure 27(c) is perfectly consistent with his results shown in the figure 27(b). I also checked the previous parameters in experiments such as QE and loss and we got good agreement.
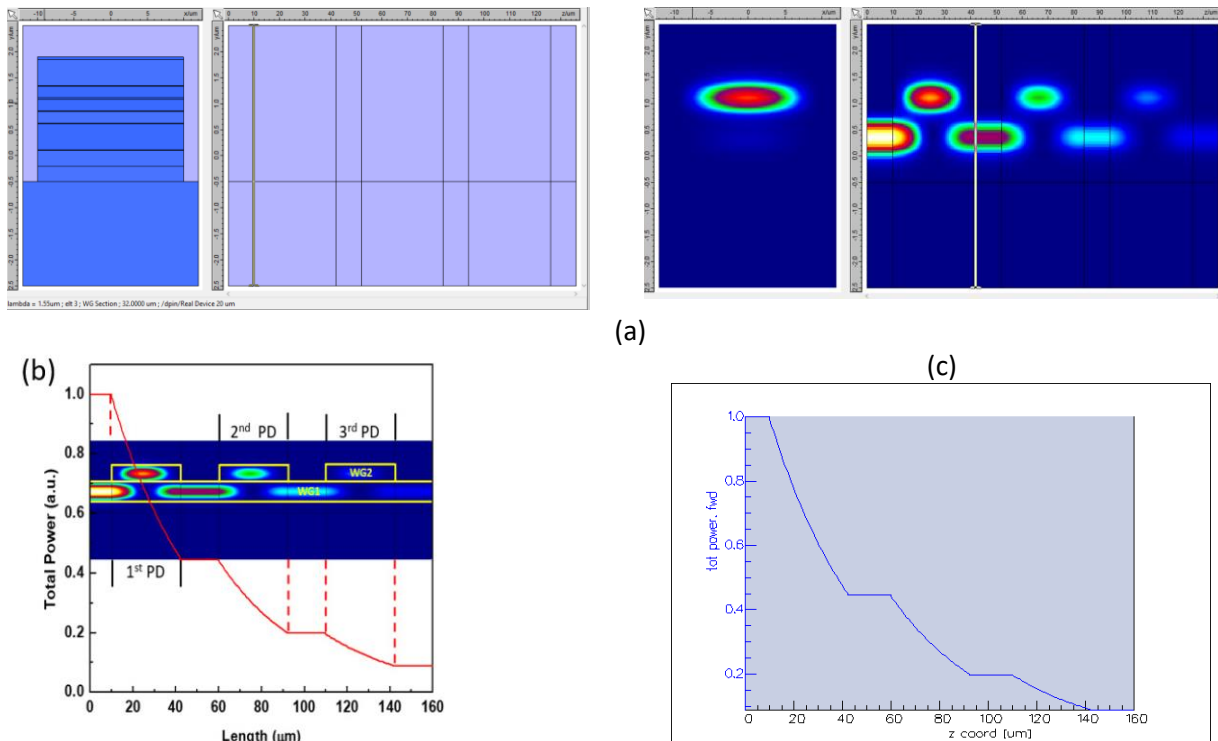

Figure 27. (a) Simulation of the total power in the segmented waveguide photodetector with 3 PDs (PD width of 20 μm, PD length of 32 μm and absorber thickness of 30 nm) by myself (b) Simulation of the total power in the Qianhuan's paper (c) Simulation of the total power by myself

When the device which the absorber width is 20 μm and absorber thickness is 30 nm for a single cycle, in this case, absolute loss a, b, and c are 0.010376, 0.533006, and 0.005247, respectively. In fact, the ratio of a, b, and c which represent the ratio account for the total power loss is much more important. The total power absolute loss δ= a+b+c is 0.548629. And I can transfer them into the A, B, and C (a/δ, b/δ, and c/δ) which is 0.018913, 0.971524, 0.009564. It can be observed that the A and C are very small, all below 0.02(2%).

A, B, and C (a/δ, b/δ, and c/δ) only have mathematical significance, as it can reflect the proportion of absolute loss for each component relative to the total loss, without any actual physical meaning. Indeed, the magnitude of the A, B, and C objectively correlates with the extent of radiation loss. A smaller A and C respectively indicates reduced radiation loss at the front and back surfaces. A larger B implies greater absorbance by the PD, consequently leading to reduced radiation loss.
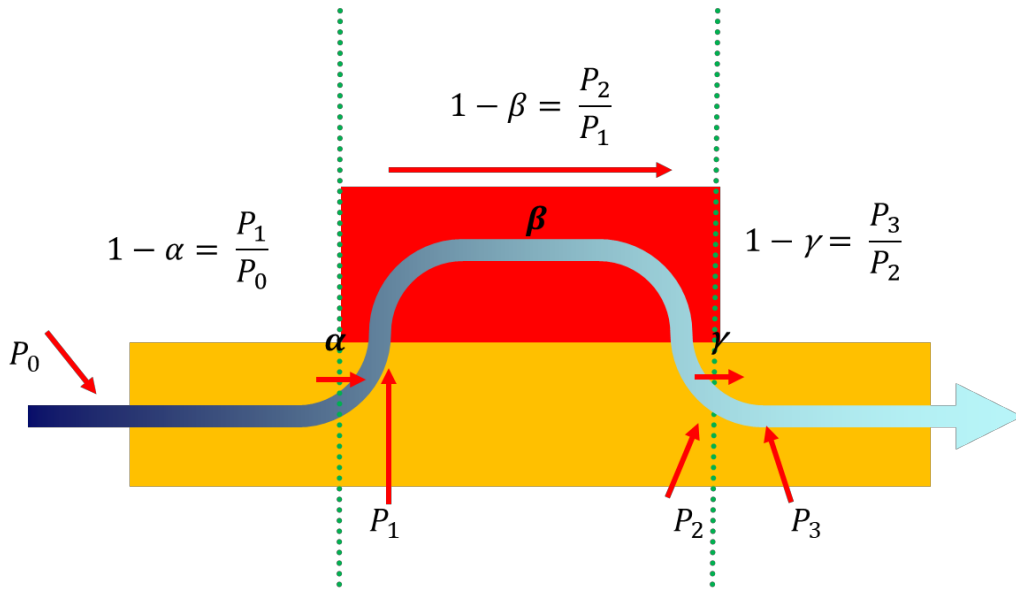
Figure 28. Loss factors α, β, and γ

For a single cycle shown in the figure 28, I can define α, β, and γ as the left loss, absorption, and right loss. The 'left loss' represents the power loss when light enters the PD from WG1 at the front end, while the 'right loss' denotes the power loss when light proceeds from the PD to WG2 at the back end. Therefore, I can define the α, β, and γ using the following equations, which have genuine physical significance and reflect the ratio of losses incurred from various surface components from incident to outgoing.

$$1 - \alpha = \frac{P_1}{P_0}$$

$$1 - \beta = \frac{P_2}{P_1}$$

$$1 - \gamma = \frac{P_3}{P_2}$$

$$(1 - \alpha)(1 - \beta)(1 - \gamma) = 1 - \delta = \frac{P_3}{P_0}$$

For example, γ reflects the ratio of power loss from the back surface, objectively representing the true magnitude of the loss. That is to say, 1-γ is equal to $\frac{P_3}{P_2}$. The smaller the γ, the less radiation loss is produced in the process from the back surface of the PD. In fact, it's quite easy to understand that the remaining power ratio at the end of one cycle, which is (1-α) (1-β) (1-γ), is equal to 1-δ, or $\frac{P_3}{P_0}$.

The β is one of the most important indicators, reflecting how much power is actually absorbed and contributes to the photocurrent rather than radiation loss. The higher the β, the higher the QE per PD. Later, I will repeatedly use this indicator to compare the efficiency of absorption in individual PD element.

Actually, in this case of a single cycle, the absolute loss a, b, and c are 0.010376, 0.533006, and 0.005247, respectively. And I can transfer them into A, B, and C (the ratio of a, b, and c), which is 0.018913, 0.971524, 0. 009564. It can be observed that both the A and C are very small, both below 0.02(2%). α, β, and γ are 0.010376, 0.538594456, 0.011491006, which can be observed that both the α and γ are also very small, both below 0.02(2%).

Therefore, I should consider that the ideal structure I desire is characterized by an extremely small α and γ, which would allow us to have a larger number of PDs. Additionally, α and γ, arising from radiation losses, should be much smaller in proportion to β to ensure feasible implementation of a larger number of PDs. Next, I can analyze the factors influencing α, β, and γ. β is related to the thickness and width and length of the absorber layer and the absorption coefficient. When the absorption coefficient and width and length of the absorber layer are fixed, it primarily depends on the thickness of the absorber layer. α is related to the thickness of the absorber layer and etching of the cladding layer. By filling the etched cladding layer, α can be reduced to a certain extent. Hence, I find that the thickness of the absorber layer is crucial—it should be extremely small. γ, given a determined thickness of the absorber layer, is mostly related to the length of the PD. Through the calculation of the supermode, I have already determined the beat length l. In fact, when the absorber length equals the beat, l, within a certain thickness of the absorber layer, its value should be minimized. Thus, under the condition of a fixed thickness of the absorber layer, I can treat γ as a constant.

When I use these three cycles, it can be observed as shown in the figure 27(c) that the total power absorption is 0.921. As shown in the figure 29, the values 0.466(46.6%) and 0.454(45.4%) represent the power proportions of the odd mode and even mode relative to the total power, respectively. The sum of these two modes corresponds precisely to the total power loss of 0.9211268(92.11268%) and, which is consistent with the remaining power 0.0788732(7.88732%) in the figure 27(c). It also means the light power absorbed in the PD is exactly the sum of the power of the odd and even modes. Moreover, it can be noticed that the power of the odd and even modes are essentially equally split. This is also due to the distributive nature of the waveguide.
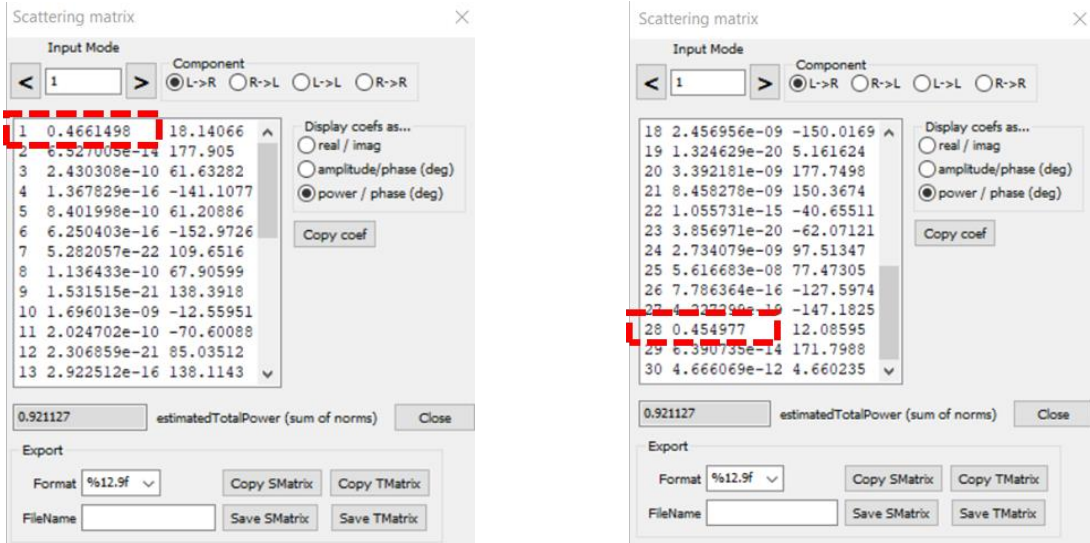
Figure 29. The odd mode and even mode relative to the total power

In fact, when multiple cycles have the same dimensions, their absorption and radiation loss remain constant. Therefore, I only need to consider the case of a single cycle.

If I turn off the absorption coefficient alpha, that is, turn off the imaginary part of the refractive index, indicates that there is no light absorption in the PD. Therefore, the power loss at the position of WG2 will be zero. At this moment, only the left loss and right loss exist. Based on the figure 30(b), the absolute left loss a is 0.0104(1,04%) and absolute right loss c is 0.0132(1.32%). Thus, the total loss can be determined to be 0.0236(2.36%), which are radiation losses, just the loss of the first row of the scattering matrix. (L→R means the transmission from the left-hand side (LHS) to the right-hand side (RHS) of the FIMMPROP Device or the selected element.) I can see that only about 97.64% of the power goes into the fundamental mode of the output waveguide, which is consistent with the total loss 2.36%. This mode is the fundamental symmetric supermode which involves the odd mode and even mode, as can be seen by inspecting them in the Mode Solver. This is consistent with the image given by the power loss, as the figure 30(c) shows.
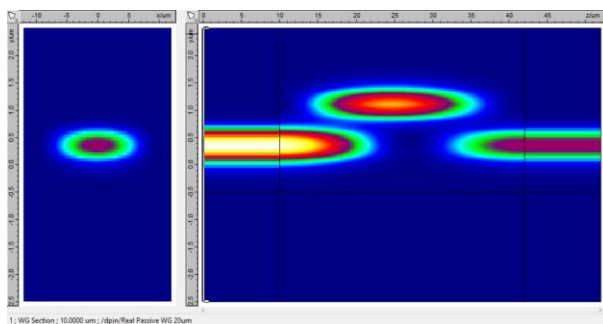
(a)
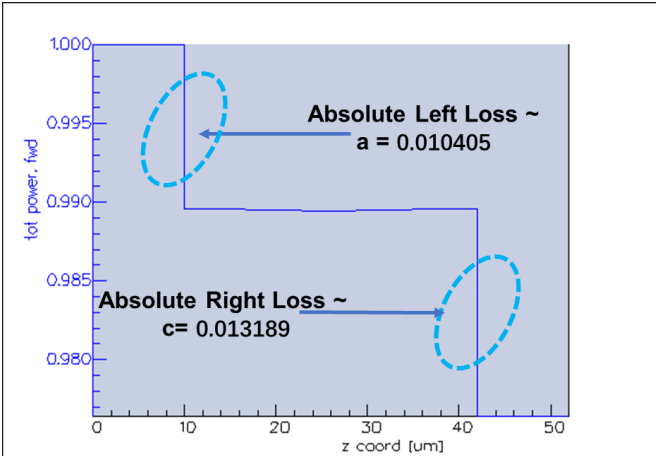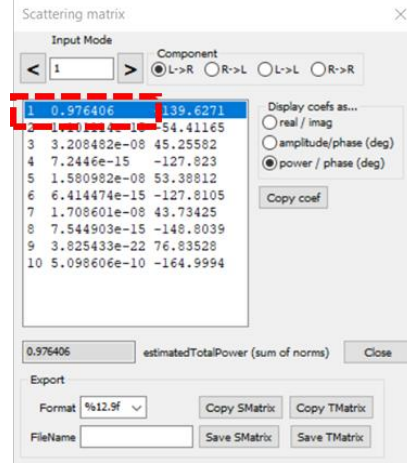
(b)   (c)

Figure 30. (a) field distribution and (b)The power loss distribution of the simulation of the total power in the single waveguide photodetector with a width of 20 µm and Length of 32 µm

In the waveguide design or coupling analysis, it is often desired to have effective refractive indices that are as similar as possible between two waveguides. When the effective refractive indices of the waveguides are similar, it facilitates efficient coupling and complete transmission of light between them. This similarity in effective refractive indices ensures a good match in the propagation constants of the waveguides, minimizing losses and maximizing the transmission of optical power. The figure 31 and 32 are the electric field distributions of the odd and even modes of the WG1 and WG2, as well as the effective refractive indices and the propagation constants beta (1/µm) in the complex form.

The WG1 is the passive waveguide and should have only one mode. I can examine the mode of the WG1 through 'WG1 Insect Mode' as the figure 31 shows. The field distribution diagram shows that the WG1 predominantly has one fundamental mode. Within this, '+ B 100' indicates that the mode in the waveguide is a TE-like mode, meaning the fundamental mode is the TE mode. Additionally, from the diagram, it is evident that the modes I obtained comprise 8 TE modes and 2 TM modes. Furthermore, I observed that the propagation constants beta of the WG1 is 13.4156 (1/µm), and the equivalent refractive index (eff index) of the WG1is 3.3095.
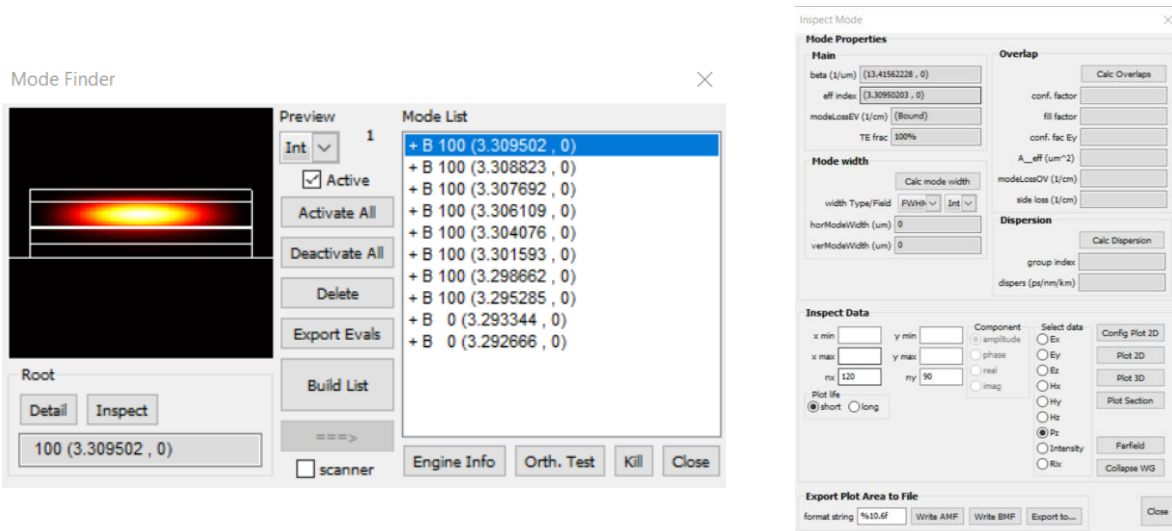

Figure 31. The WG1 Insect Mode

The WG2 serves as the PD and should have two modes. I can use the 'WG2 Insect Mode' to observe the modes of the WG2. The distribution diagram indeed shows that it has two modes: the odd mode and the even mode as the figure 32 shows.
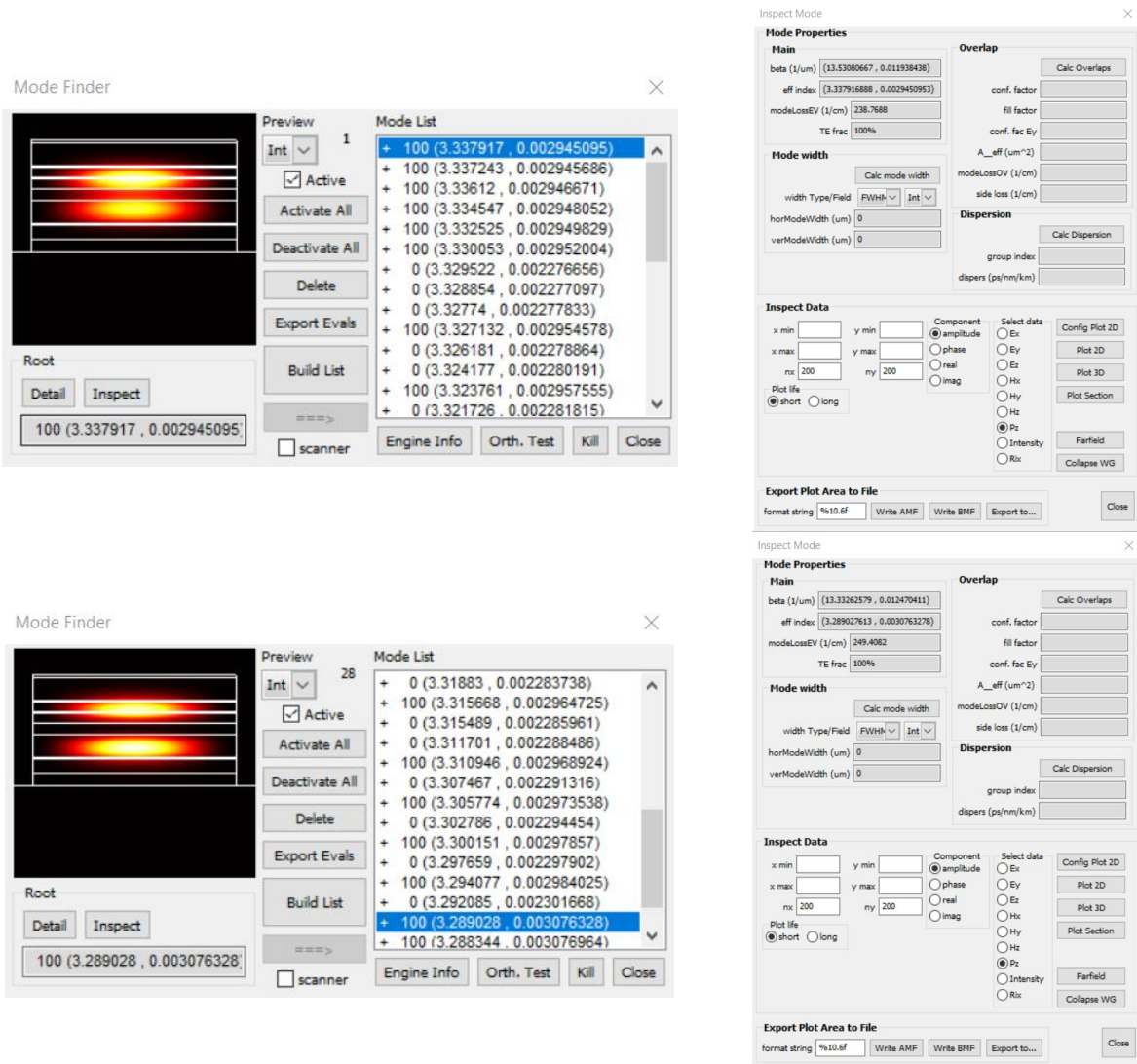

Figure 32. The WG2 Insect Mode

Moving forward, my primary focus will be on the propagation constants beta (1/μm) and its real and imaginary components, analyzing how to minimize its losses. When I choose the first mode as the TE mode (which will be referred to as the even mode in subsequent discussions), the real and imaginary parts of beta are (13.53080667, 0.011938438). The real and imaginary components of the equivalent refractive index (eff index) are (3.337916888, 0.0029450953). When the real and imaginary parts of the eff index of WG1 and WG2 are matched, or are extremely close to each other, the minimization of radiation loss can be achieved. This is a key benchmark I utilized during the optimization process.

When I select the TE mode of the 28th mode (which will be referred to as the odd mode in the following text), the real and imaginary parts of beta are (13.33262579, 0.012470411). The real and imaginary components of the equivalent refractive index (eff index) are (3.289027613, 0.0030763278). To

achieve a match in the real and imaginary parts of beta or the equivalent refractive index, the even mode and odd mode of the WG must correspond to each other. Additionally, they should match with WG1's propagation constants beta, which is 13.41562228(1/μm), and its equivalent refractive index eff index, which is 3.30950203.

Intensity of even mode   Intensity of odd mode

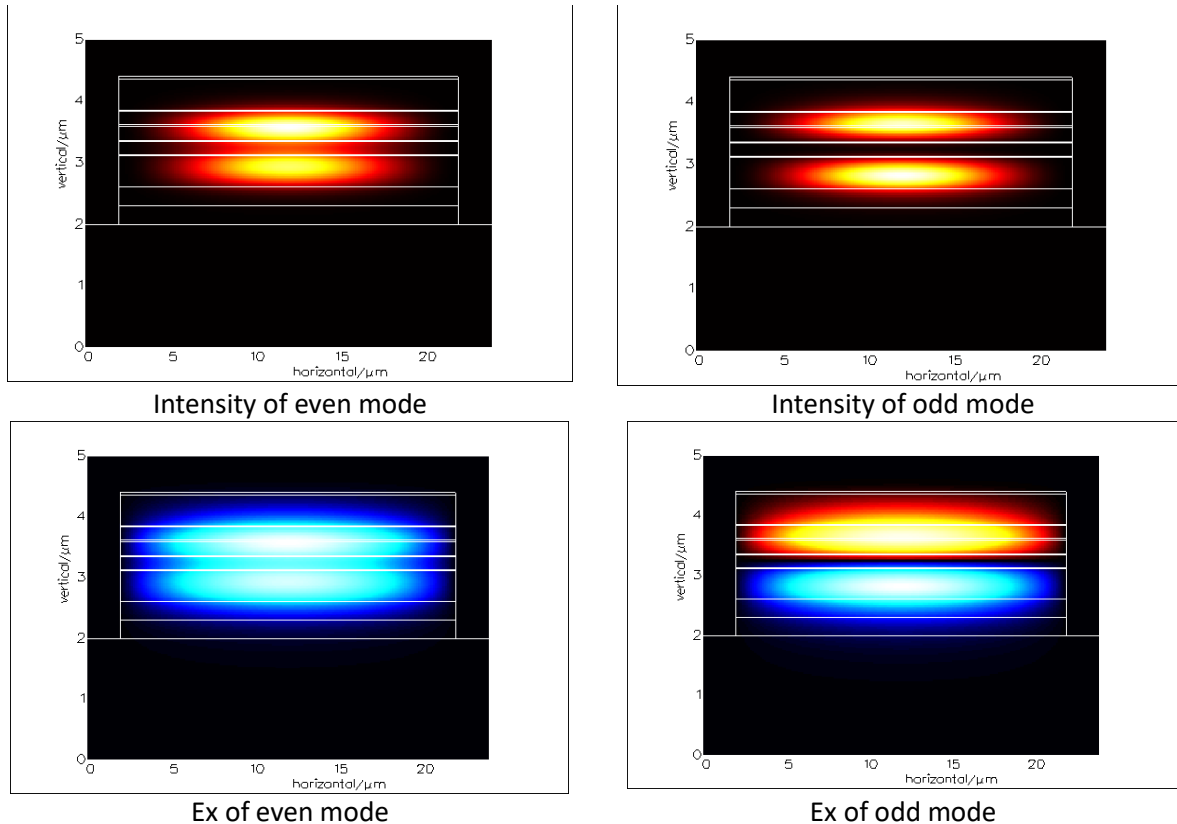Ex of even mode   Ex of odd mode

Figure 33. Intensity and Ex of even mode and odd mode

I can observe the distribution of the even mode and odd mode through the 'Intensity and electric field distributions of even mode and odd mode' as the figure 33 shows. The intensity distributions of both the even mode and odd mode are symmetric. However, while the Ex-distribution of the even mode is symmetric, the Ex-distribution of the odd mode is precisely the opposite. This is consistent with the definitions of even mode and odd mode.

4.3 Optimization of PD width

In fact, propagation occurs along the z-direction, so the width of the PD should not significantly affect the quantum efficiency (QE) and device efficiency. To verify this, when calculating the efficiency for a single cycle, I can choose different PD widths, such as 5μm, 15μm, and 20μm, and calculate them independently. This comparison can help us understand the impact of different PD widths on the device's performance. By calculating multiple PD widths, I can identify the optimal PD width to achieve higher quantum efficiency.

It can be observed that as the width decreases, the parameter α also diminishes. The resulting power graph and field distribution diagram are shown in the figure 34. When the width is 2μm, the field distribution is already distorted, whereas at 30 μm width, it is also displaying a distorted field distribution

from the WG1 to the WG2 and then back to the WG1. Both of these situations should be avoided as much as possible.

single device 2 μm width   single device 5 μm width   single device 10 μm width

single device 15 μm width   single device 20 μm width   single device 30 μm width
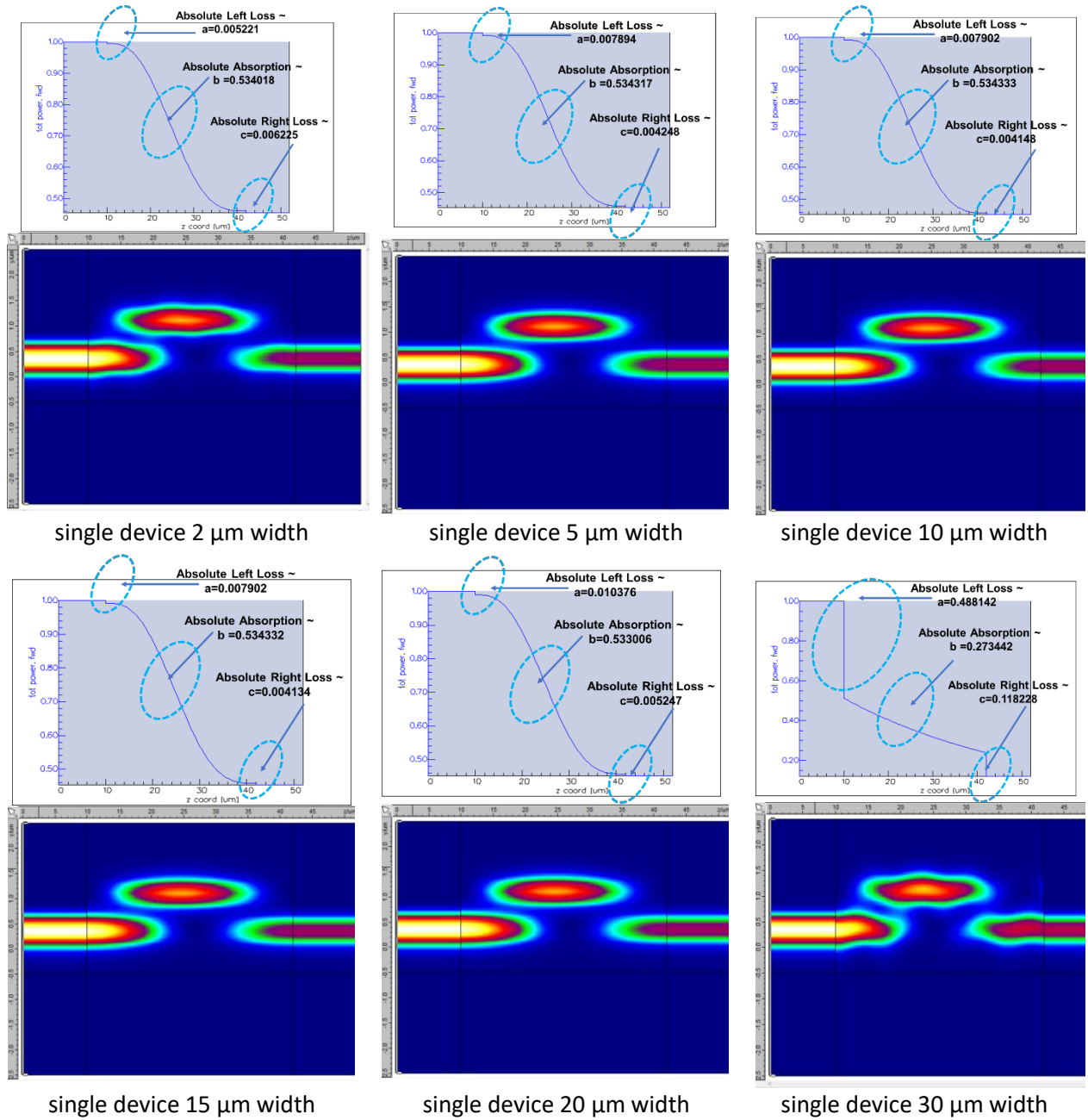
Figure 34. The resulting power graph and field distribution diagram

Thus, I can retrieve the optimized values of a, b, and c based on width and then convert them into A, B, and C, as well as the α, β, and γ, as mentioned in section 4.2, as shown in the table 2.

Table 2. Optimized values of α, β, and γ based on width

Width(μm)	1	2	5	10	15	20	30
a	0.009476	0.005221	0.007894	0.0079	0.007902	0.010376	0.488142
b	0.428303	0.534018	0.534317	0.534333	0.534332	0.533006	0.273442
c	0.07607	0.006225	0.004248	0.004148	0.004134	0.005247	0.118228
Total Power Loss δ	0.513849	0.545464	0.546459	0.546381	0.546368	0.548629	0.879812
A	0.018441	0.009572	0.014446	0.014459	0.014463	0.018913	0.554825
B	0.833519	0.979016	0.977781	0.977949	0.977971	0.971524	0.310796
C	0.14804	0.011412	0.007774	0.007592	0.007566	0.009564	0.134379
α	0.018441	0.009572	0.014446	0.014459	0.014463	0.018913	0.554825
β	0.833519	0.979016	0.977781	0.977949	0.977971	0.971524	0.310796
γ	0.14804	0.011412	0.007774	0.007592	0.007566	0.009564	0.134379

Based on the table, which highlights the lowest numbers for the loss, I can derive the figure 35 showing the variation of A, B, and C, as well as the α, β, and γ with respect to the change in width.
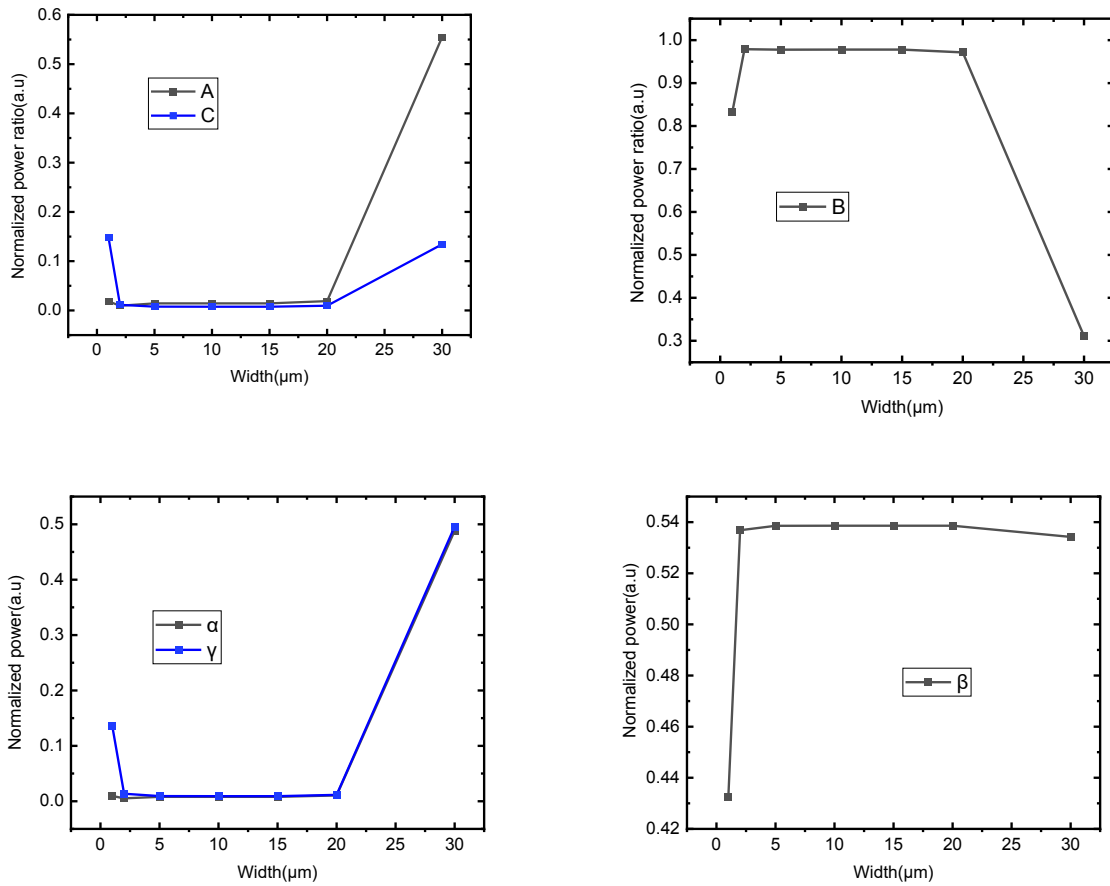

Figure 35. The effect of width variation on the A, B, and C, and the α, β, and γ

The figure 35 illustrates the effect of width variation on the A, B, and C, and the α, β, and γ. It indicates that within the width range of 5 to 15µm, the B remains optimal and is essentially flat at the same high level of 97%. Similarly, within the width range of 5 to 20µm, the α remains at the same flat low level (α =1.44%), and the γ also maintains at the same flat low level (γ =0.75%). Thus, the width within the 5 to 20µm range can be identified as the optimal dimension following optimization.

Since the width of the passive waveguide section is same as the PD sections, it can be explained that the ideal width is dictated by the coupling match between waveguides WG1 and WG2. Excessively large widths elevate radiation losses, due to mode mismatch. Conversely, overly narrow widths could impede complete mode transmission, also resulting in elevated radiation losses for the same reasons. Consequently, the optimal width should be aligned with the light path width within the waveguide. It should neither fall below the modal width, to avoid modal losses, nor exceed it, to prevent radiation losses. For example, when the width is 30µm, the electric field distribution as illustrated indicates a significant mismatch in the coupling between WG1 and WG2, leading to a sharp drop in the B and β.

The FIMMPROP Scanner can study the evolution of the results when varying arbitrary parameters of the structure. Thus, I also employed a FIMMPROP scanner to examine the PD width, as shown in the figure 36. Consistently, it was observed that within the width range of 5 to 20µm, the power loss per cycle remains constant. This finding is in alignment with my previous width optimization results, further substantiating the selection of a width within the 5 to 20µm range as optimal. Therefore, in the following steps, I can select a width in the range of 5 to 20µm to ensure optimal absorption. Notably, the peak performance is observed at a width of 15µm, which is also the optimal width I chose later on.
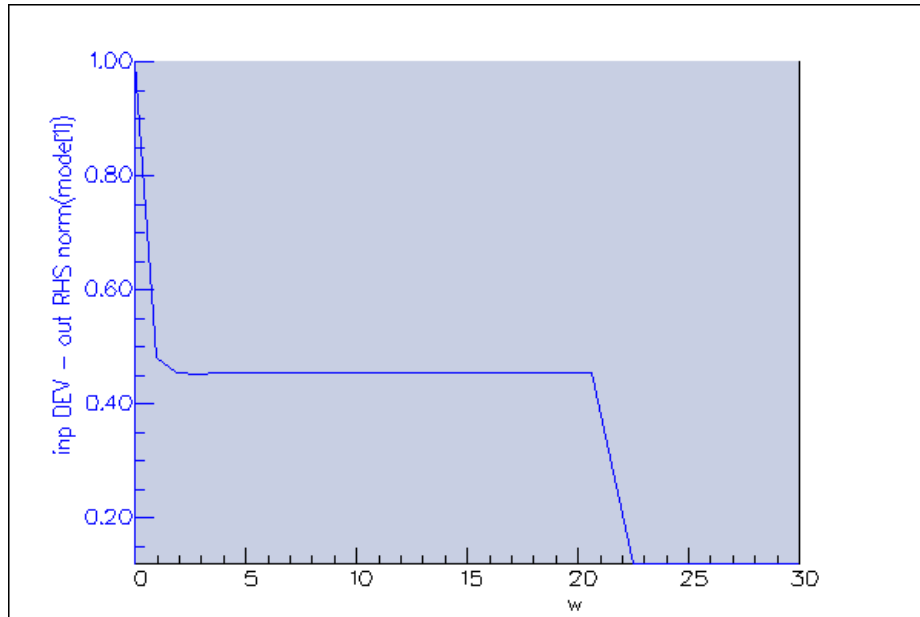

Figure 36. The FIMMPROP scanner of PD width

4.4 Optimization of PD length

The PD length is one of the most critical factors affecting α, β, and γ, and it also plays a significant role in the mode matching between the WG1 and WG2. Previously, I introduced the concept of "beat length",

denoted as l, which is defined as $l = \frac{2\pi}{\Delta\beta_r}$. In practice, the PD length should be an integer multiple of the beat length to minimize radiation loss.

In this study, however, I did not utilize this formula to calculate the beat length. This is because FIMMWAVE allows me to directly optimize the PD length using the FIMMPROP scanner, thereby providing a visual representation of the optimization effects, and reducing computational redundancy.

When I choose 15µm as the width for the PD, I can use the FIMMPROP scanner to select a PD length ranging from 0 to 220µm for the device's power input-output diagram. The results, as illustrated in the accompanying figure 37, reveal that the total power loss is maximized when the PD length is at 32µm,64µm, or 96µm. From the modal field plots, it is also evident that there is one, two, or three modes in the PD at these lengths, respectively. Thus, I have chosen PD lengths that are integer multiples of the beat length for analyzing variations in α, β, and γ.
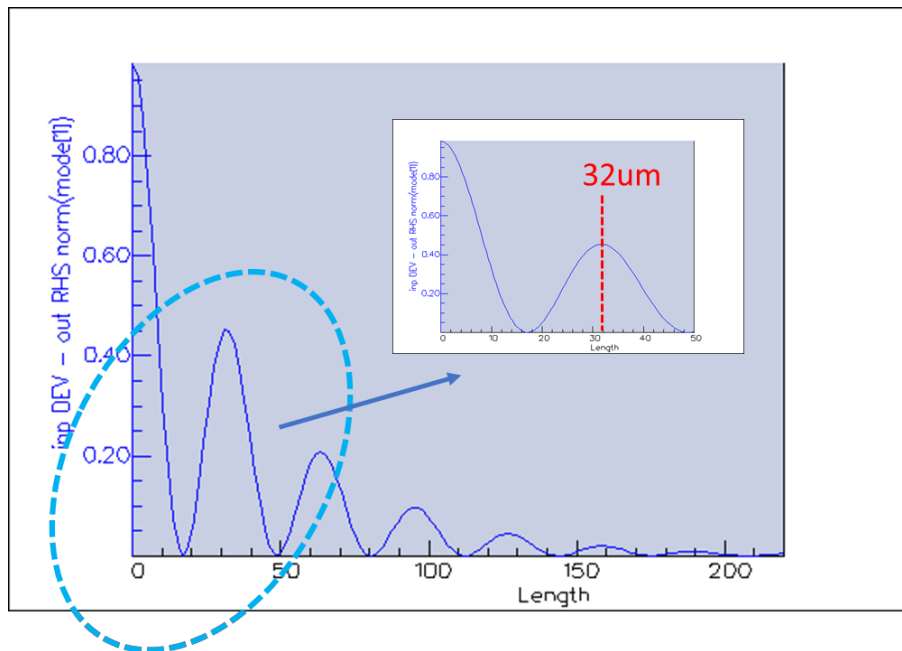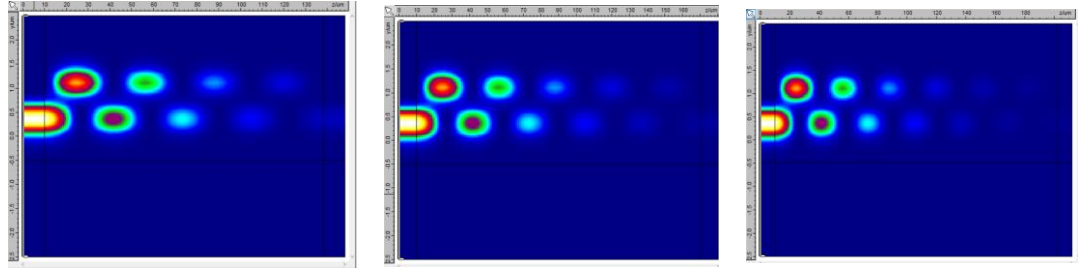

Figure 37. The FIMMPROP Scanner of PD Length

The field distribution diagrams are shown in the table 3.

Table 3. The field distribution diagram for N*Length

	device 15µm single Length	device 15µm 2*Length	device 15µm 3*Length
PD length	32.0313µm	2*32.0313µm	3*32.0313µm
Filed distribution			
PD length	4*32.0313µm	5*32.0313µm	6*32.0313µm

Filed distribution

Thus, I can also the optimized values of a, b, and c based on length and then convert them into A, B, and C, as well as the α, β, and γ, as mentioned in section 4.2, as shown in the table 4.

Table 4. Parameters for N*Length

Length	L	2L	3L	4L	5L	6L
a	0.00793	0.007927	0.007929	0.007931	0.007933	0.007934
b	0.534307	0.780795	0.894537	0.947036	0.971272	0.982462
c	0.004222	0.002655	0.001762	0.001154	0.000731	0.000447
Total Power Loss δ	0.546456	0.791377	0.904228	0.956121	0.979936	0.990843
A	0.014506	0.010017	0.008769	0.008295	0.008095	0.008007
B	0.977768	0.986628	0.989283	0.990498	0.991159	0.991541
C	0.007726	0.003355	0.001948	0.001207	0.000746	0.000451
α	0.00793	0.007927	0.007929	0.007931	0.007933	0.007934
β	0.538578	0.787034	0.901686	0.954607	0.979039	0.990319
γ	0.009223	0.012566	0.018065	0.025626	0.035153	0.046543

It is easy to understand that the value of α remains unchanged, as increasing the length does not alter the pathway from WG1 to WG2. Therefore, only b, and c are affected: b will increase, while c will also increase.

Based on the table, I can derive the graph showing the variation of A, B, and C, as well as the α and β with respect to the change in width, as shown in the figure 38.
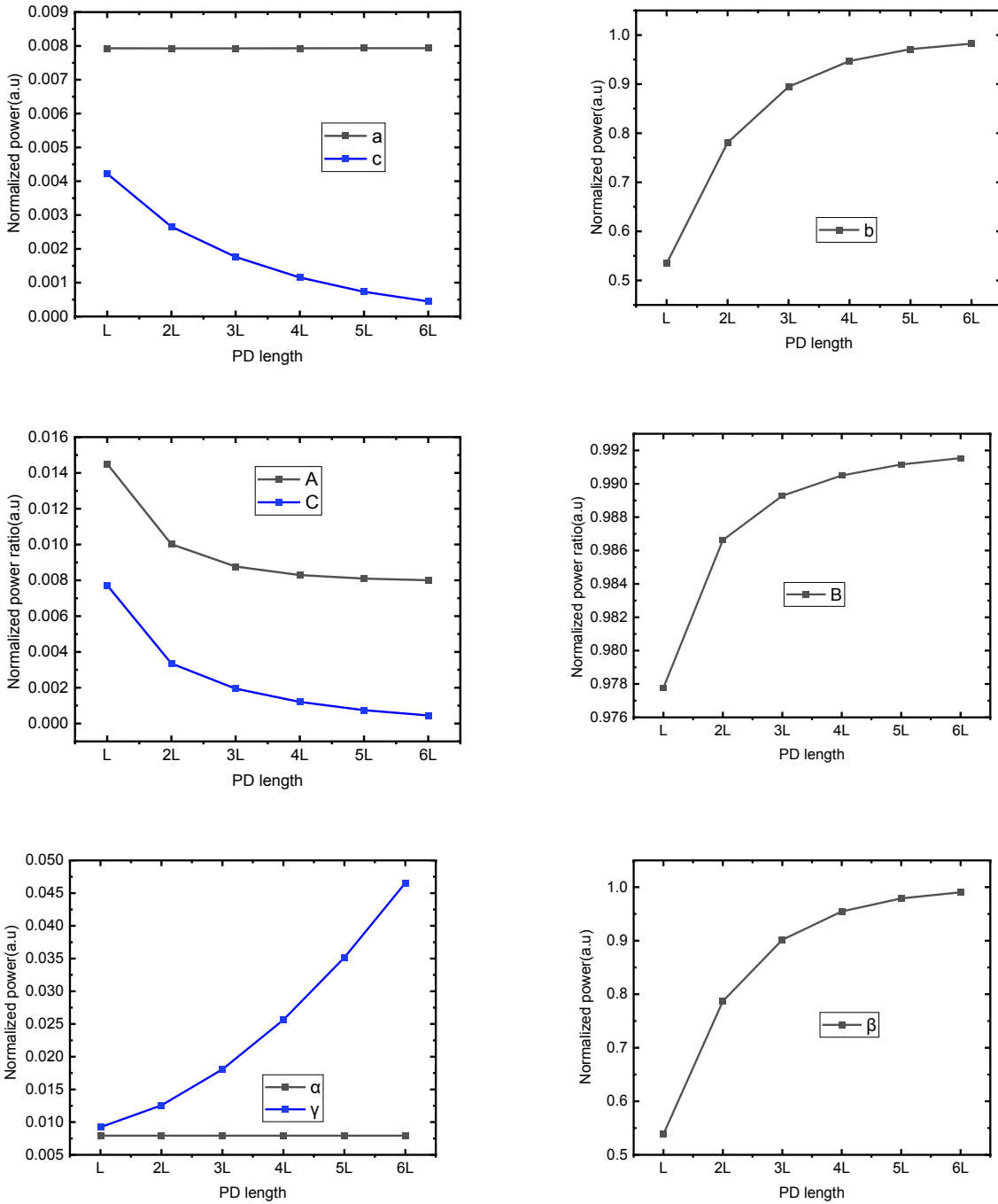
Figure 38. The effect of PD length variation on the a, b, and c, A, B, and C, and the α, β, and γ

The figure 38 illustrates the effect of length variation on a, b, and c, A, B, and C, as well as the α, β, and γ. It indicates that the a remains constant. This is easily understood since changing the length would not alter the front-end loss but only affects the back-end loss. As the length increases, the b becomes larger, but its rate of growth diminishes. As the length increases, c decreases, but the rate of its decrease gradually diminishes.When transformed into A, B, and C, A and C decreases at a decreasing rate, whereas

B increases but at a decelerating pace. In terms of the real values, as the length increases, α remains constant, while γ increases at an increasing rate. Simultaneously, β increases at a diminishing rate. From this, to minimize radiation loss, the length should be chosen as the beat length L, which is the single cycle's length L.

When γ is determined by the thickness of the absorber layer, it is solely dependent on the length of the PD. Through the calculation of supermode, I have already discovered the beat length, l. In fact, when γ equals the beat length, l, within a single period, its value should be minimized. Therefore, in the following simulations, under the condition of a certain PD length (equal to the beat length), I can treat γ as a fixed value.

4.5 Optimization of PD absorber thickness

In the Rajveer Nehra's paper [2], to further reduce the radiation loss and enable segmented detectors with larger PD count which is designed by a new structure and made two changes compared to: (i) adding an additional cladding layer on top of the passive waveguide WG1, and (ii)reducing the thickness of the absorber layer from 30 nm to thinner thickness.

I can reduce the radiation loss and enable segmented detector in both of these two ways.

From this figure 39, I can see that the change of PD absorber thickness is positively related to absorption, so the smaller the PD absorber thickness, the better of the performance. I can take the minimum to 1nm.
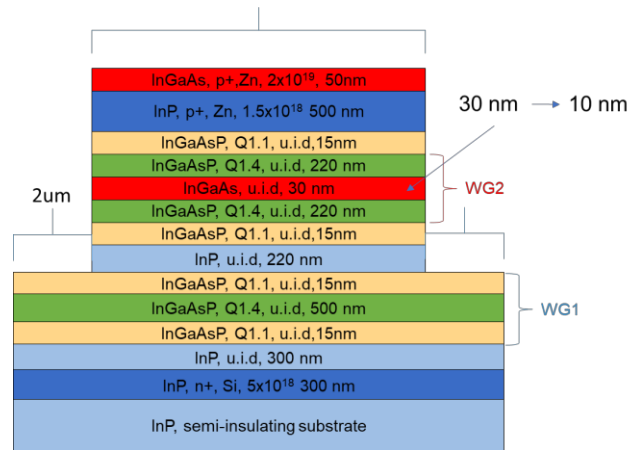

Figure 39. Schematic diagram of changing PD absorber thickness

Building upon a base width of 15μm, I further optimized the InGaAs PD absorber thickness. I selected thickness values of 30 nm,10 nm,6 nm,3 nm,2 nm, and 1 nm for investigation, subsequently obtaining the corresponding values for the α, β, and γ. The results are presented in the following table 5.

Table 5. Parameters for different PD absorber thickness

PD absorber thickness (nm)	30	10	6	3	2	1
a	0.00793	0.007244	0.007124	0.007029	0.006998	0.006967
b	0.534307	0.201557	0.122004	0.061185	0.040805	0.020404
c	0.004222	0.006751	0.006694	0.007078	0.006705	0.006632
Total Power Loss δ	0.546459	0.215552	0.135822	0.075292	0.054508	0.034003
A	0.014512	0.033607	0.052451	0.093357	0.128385	0.204894
B	0.977762	0.935074	0.898264	0.812636	0.748606	0.600065
C	0.007726	0.03132	0.049285	0.094007	0.123009	0.195042
α	0.00793	0.007244	0.007124	0.007029	0.006998	0.006967
β	0.538578	0.203028	0.122879	0.061618	0.041093	0.020547
γ	0.009223	0.008533	0.007687	0.007596	0.007042	0.006819

Through curve fitting in the figure 40, I was able to discern the relationship of these figures of merit with respect to the PD absorber thickness. The results reveal that as the PD absorber thickness decreases, the a increases linearly, the c generally decreases, and the b exhibits a linear growth relative to the PD absorber thickness. Additionally, as the length increases, both the A and C decrease, while the B rises. When looking at the α, β, and γ, as the length increases, the α grows and sees intense variations around 5nm, whereas the γ rises linearly, displaying a direct proportional relationship. Simultaneously, as the length increases, the β also almost linearly rises, maintaining a direct proportional relationship. It's evident that, to minimize radiation loss, a thinner PD absorber is more effective.
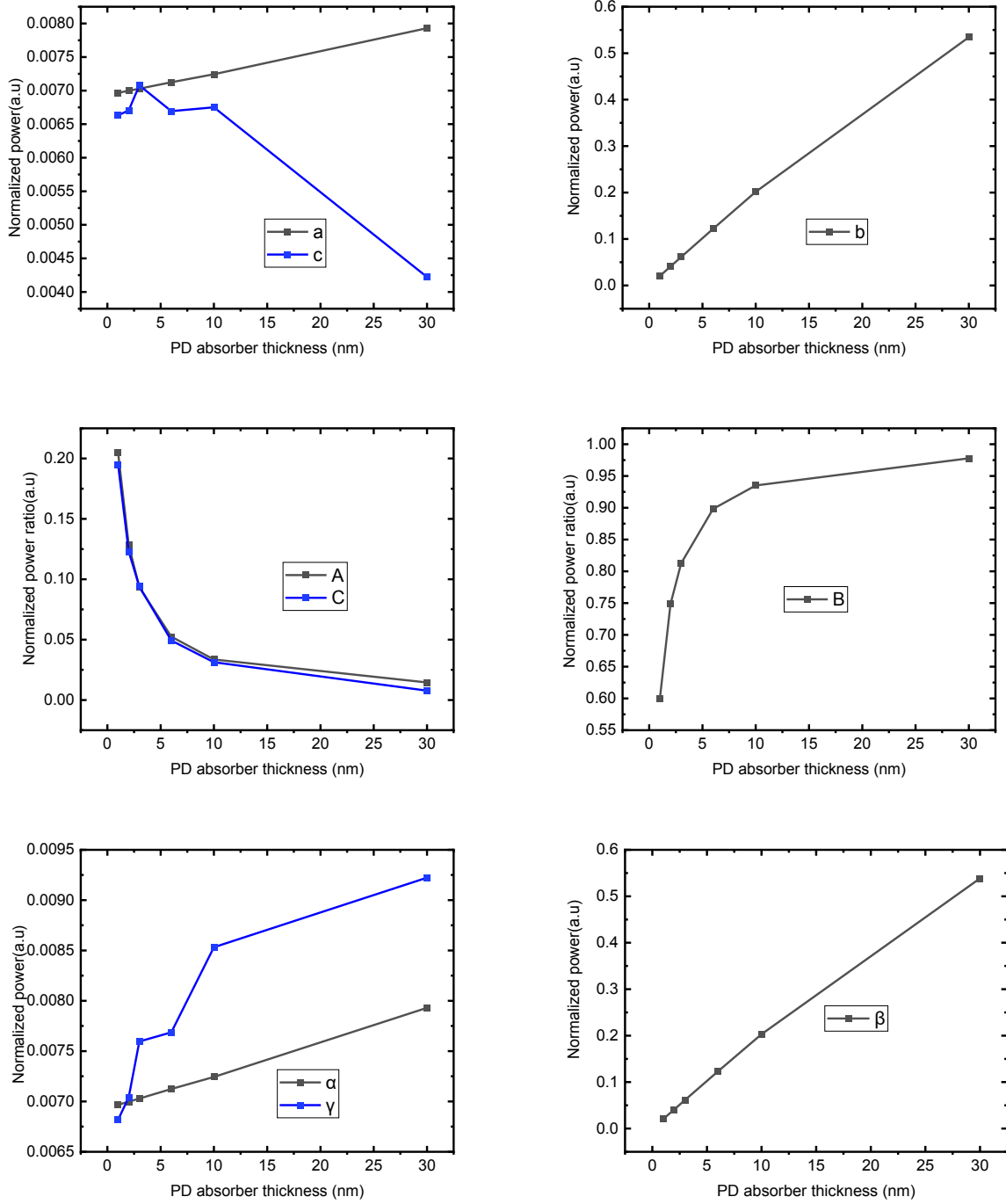
Figure 40. The effect of PD absorber thickness on the a, b, and c, A, B, and C, and the α, β, and γ

Similar to the width optimization scan, I utilized the FIMMPROP Scanner to optimize the PD absorber thickness. The scan ranged from 0 to 10 nm and revealed that the power loss per cycle decreases as the thickness diminishes as shown in the figure 41. Therefore, the selected PD absorber thickness should be as small as possible, though it cannot be infinitely small. I settled on a PD absorber thickness of 1 nm.

Under these conditions, the α, β, and γ values were found to be 0.0069(0.69%),0.0205(2.05%), and 0.0066(0.66%), respectively. This simultaneously effectively reduced the sum of the A and C to below 40%.
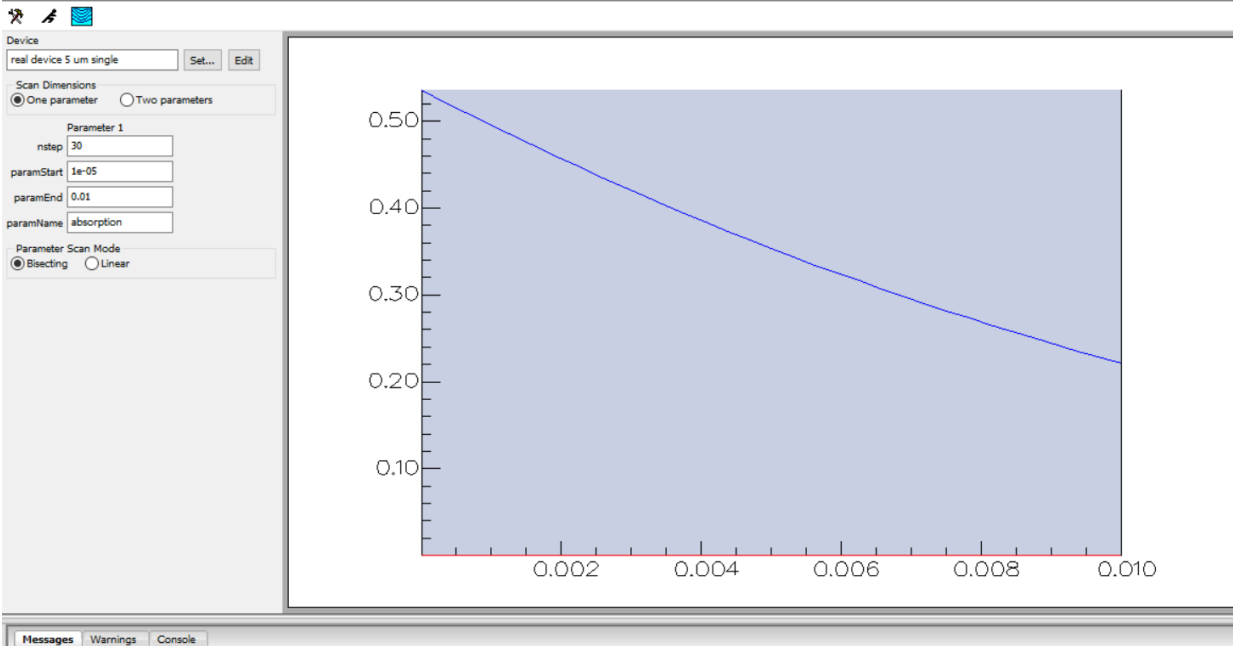

Figure 41. The FIMMPROP Scanner of PD absorber thickness

There exists an inherent contradiction in the requirements: on one hand, a smaller β is desired to accommodate a greater number of PDs; on the other hand, a larger β is also sought to maintain reasonable QE in each PD element. To resolve this, I will later employ the method of etching the cladding layer to enhance the β. Through curve fitting, it can be concluded that the minimum α and γ occurs when the PD absorber thickness is 1nm, representing the condition under which both α and γ are best optimized.

$$\text{Power Loss } \delta = 0.034003$$

$$\text{Remaining Power ratio} = (1 - \delta)^N < 0.001$$

By establishing the given setting ratio, I arrive at the final usable power loss, which is analogous to the definition of the image resolution. The term 'resolution' refers to the measuring or display system's ability to distinguish details, or the smallest discernible size in an image. In this context, the setting ratio represents the smallest amount of power loss that can be consumed by radiation loss. After calculations conducted in MATLAB, the total loss needs to be less than 0.001, allowing for as many as 199 PDs, as shown in the figure 42.
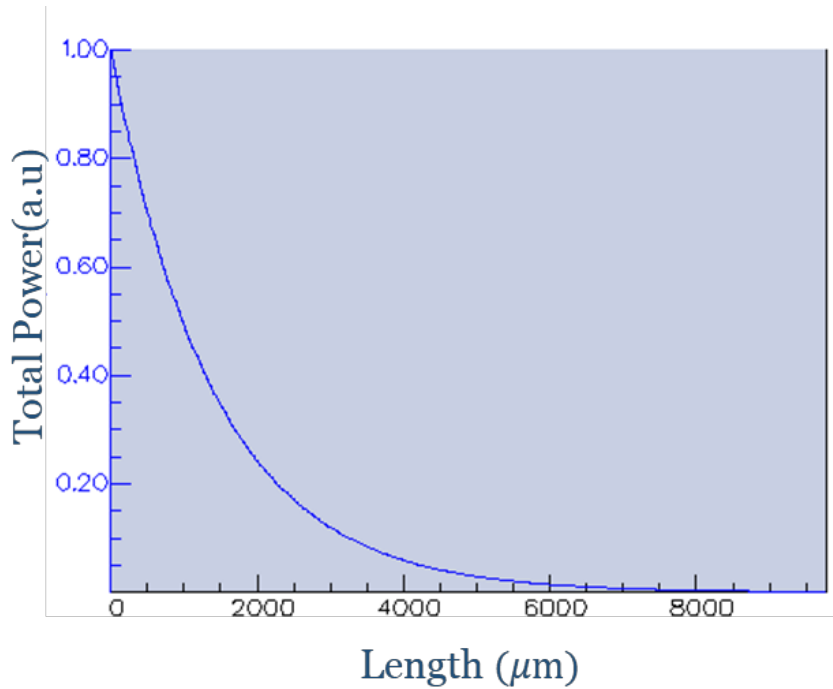
(a)
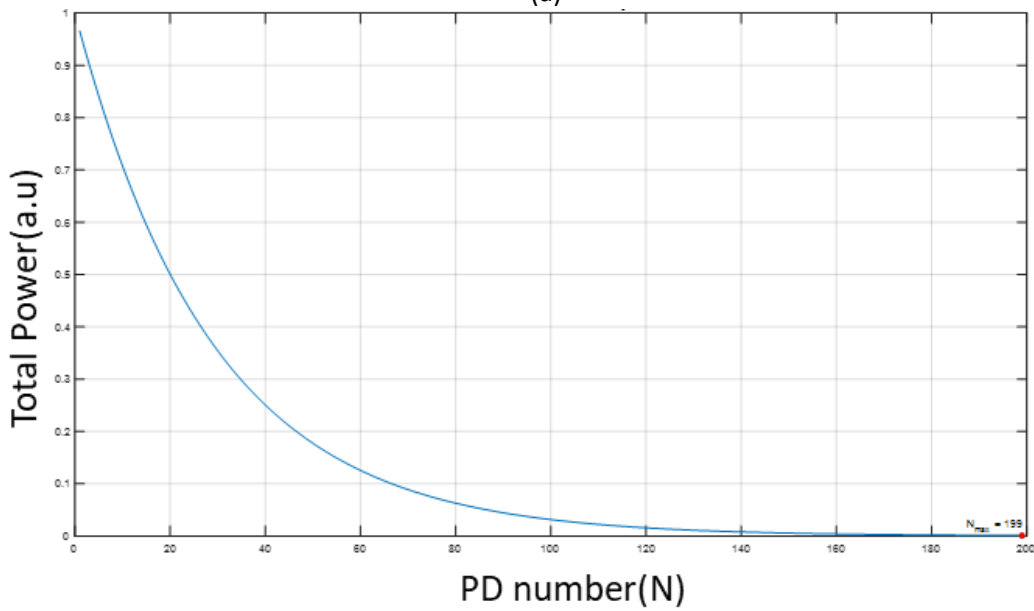
(b)

Figure 42. The variation in power of 199 PDs in relation to (a) the z-axis distance and (b) the PD number.

These factors contribute to the determination of the total quantum efficiency (QE) of the photodetector.

I use the following equation to estimate the total QE for a system of segment PDs. The equation is given by:

$$PD_{1n}(x + 1, \eta_{out}, \eta_{in}) = PD_1 + \sum_{n=1}^{x} \left[(T(\eta_{out}, \eta_{in}))^n \cdot (\eta_{in} \cdot QE) \right]$$

Where:

- $PD_{1n}(x+1, \eta_{out}, \eta_{in})$ represents the total quantum efficiency after $x+1$ segments of photodetectors.

- PD_1 is the product of η_{in} and QE for the first photodetector (the input photodetector).

- QE is the quantum efficiency of each individual photodetector.

- T is the transmission through one segment, given by $T = [\eta_{in} \cdot (1 - QE) \cdot \eta_{out}]$.

- η_{in} represents the "1-α" (α is the left loss), which is the efficiency of transmitting light into a photodetector segment.

- η_{out} represents the "1- γ" (γ is the right loss), which is the efficiency of transmitting light out of a photodetector segment.

The equation calculates the total quantum efficiency of the entire photodetector system when the photodetectors are connected in series, accounting for the losses at each stage. The total QE is calculated by adding the QE of the first photodetector (PD_1) with the QE contributed by each subsequent photodetector segment, considering the losses (left loss and right loss) between the segment PDs.

So I can calculate the total quantum efficiency after 199 segments of photodetectors as shown in the figure 43. The result shows that the total QE of the 199 PDs is 59.94%. I have pretty low loss, only 0.6%, but I still did not get the full QE, flattening out at 60%, which is not very high, indicating that there is further room for optimization of loss.
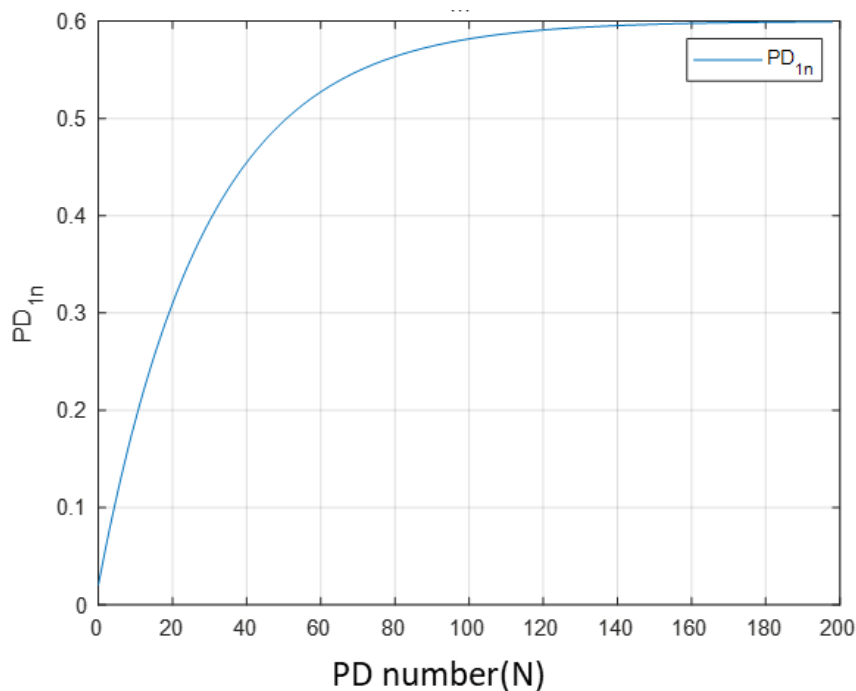

Figure 43. The total QE VS the 199 PDs

4.6 Optimization of etching cladding layer

Due to the light path transmission from WG1 to WG2 and back to WG1, the upper edge of WG1 is not directly involved in the optical routing. Thus, completely etching WG1 down to its current state could result in contact with air and subsequent radiation loss. On the other hand, partial etching presents the issue of determining the optimal etch depth for the cladding layer. Failing to etch the cladding layer at all would essentially equate to a multiple of the beat length, which would not fully utilize the potential of WG1. Therefore, it is imperative to optimize the etch depth of the cladding layer to make the etching process reasonable while minimizing radiation loss as shown in the figure 44.
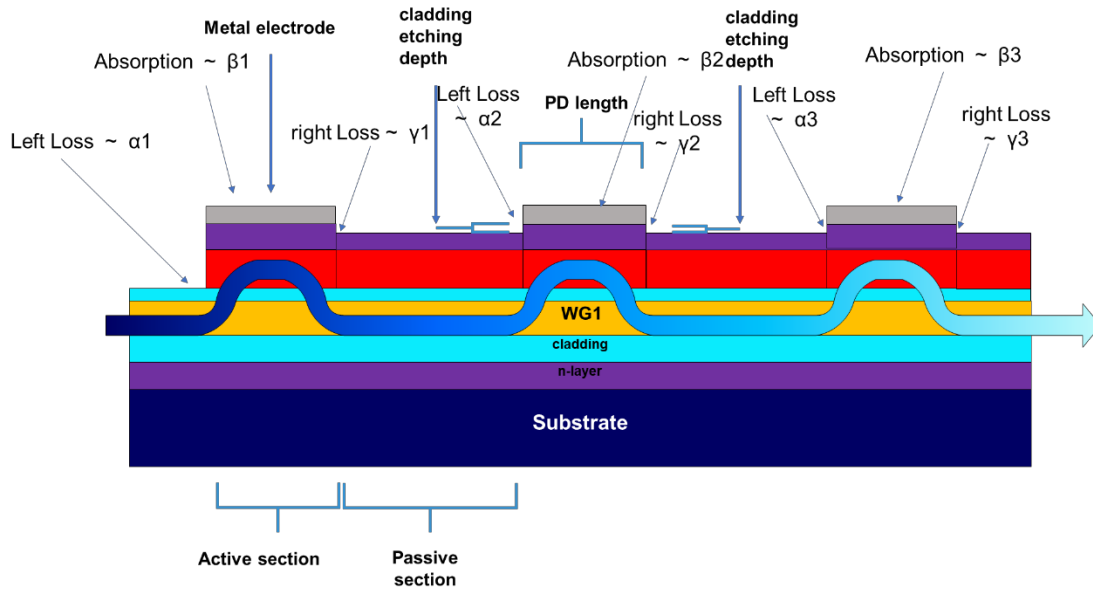

Figure 44. Schematic diagram of parameter of Etching cladding layer

I selected the PD width of 5 µm and the PD absorber thickness of 30 nm to analyze the effects of etching the cladding layer. First, I used a length FIMMPROP Scanner to determine that the beat length under these conditions is 31.31 µm as shown in the figure 45. Consequently, I set the PD length for all devices to 31.31 µm.
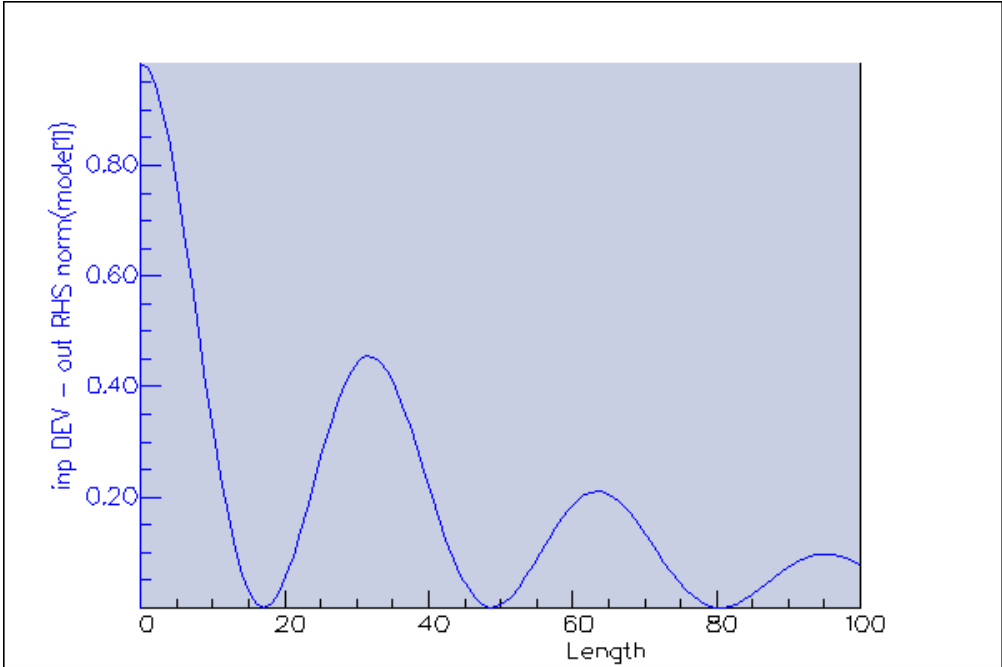
Figure 45. The FIMMPROP Scanner to determine that the beat length

As the figure 46 shows, my etching of the upper cladding layer starts directly after the first PD and does not include the very first PD. The same etching conditions are applied between every two PDs thereafter.
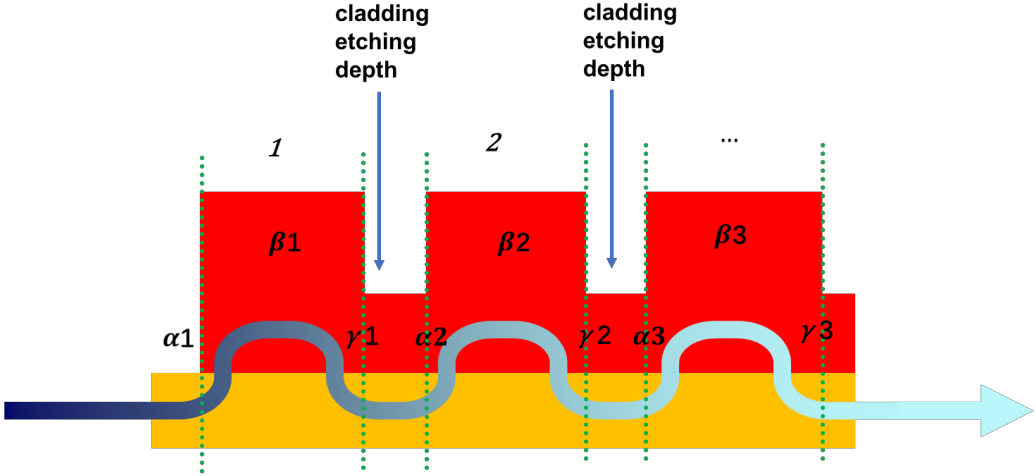

Figure 46. Loss of the Schematic diagram of etching cladding layers

So, it's easy to see the following relationships:

$$\alpha 1 \neq \alpha 2 = \alpha 3$$

$$\beta 2 = \beta 3$$

48

$$\gamma 2 = \gamma 3$$

I can simplify this optimization by configuring a scenario with three PDs., where WG1 remains as a passive waveguide. The original setup corresponds to completely etching down to the underlying InGaAsP Q1.1 layer, with an etching depth of 1050 nm. The power loss can give that the α, β, and γ are 0.0103(1.03%), 0.533(50.33%), and 0.0052(0.52%), respectively.

To etch the cladding layer, I first examined the top structure of the PD. In fact, the three-layer structure of InGaAsP Q1.4, InGaAs, and InGaAsP Q1.4 constitutes the core structure of WG2. Therefore, I can etch the layers from top to bottom, but without reaching WG2. The etching cladding layers including InGaAs, InP, and InGaAsP Q1.1, as shown in the figure 47, with varying thicknesses to minimize radiation loss.
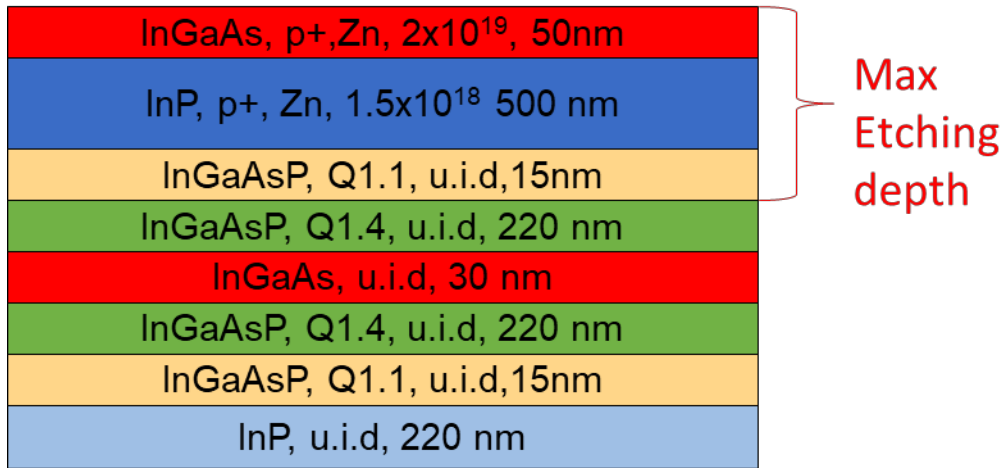

Figure 47. Schematic diagram of etching cladding layers from top to bottom

Firstly, when I completely etch away the upper cladding layer InGaAsP Q1.1, the etching depth is 565 nm. When I partly etch away the InGaAsP Q1.1, for example, the etching depth is 560 nm. Secondly, when I completely etch away the InP layer, the etching depth is 550 nm. When I partly etch away the InGaAsP Q1.1, the etching depth, for instance, is 350 nm. When I completely etch away the InGaAs layer, the etching depth is just 50 nm. Finally, when I partly etch away the InGaAs layer, the etching depth is 40, 30, 20, 10 nm, respectively. From this optimization, I can determine the absolute power loss values a, b, and c, as well as the α, β, and γ.

It can be observed in the figure 48 that when the etching has not reached the InP layer, and is only at the InGaAs layer depth, the B2 is almost always very high, exceeding 0.999(99.9%) which meets the requirement for reducing radiation loss. Moreover, both the α2 and γ2 have dropped to the E-05(0.001%) level, which is two orders of magnitude smaller than the previous result. Such results can be described as a significant breakthrough.
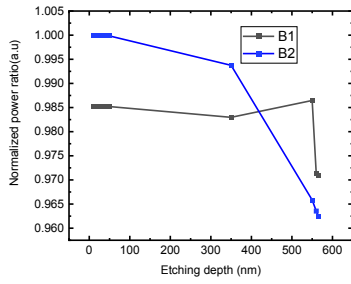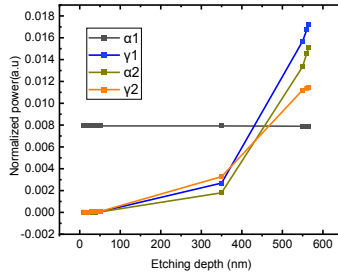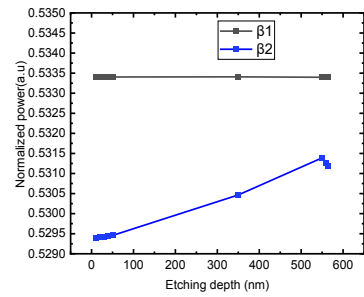
B1, B2   α1, α2, γ1, γ2   β1, β2

Figure 48. The effect of the etching cladding layer depth on the B, α and β and γ in 50nm PD absorber thickness

Subsequently, I selected a range for the PD absorber thickness between 1-5nm. I then carried out the same etching processes and plotted the fitting curves for the B, α, β, and γ with the etching cladding layer depth ranging between 10-565nm. The results are presented in the following table 6.

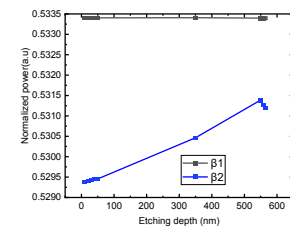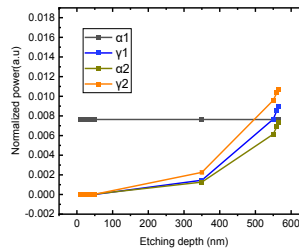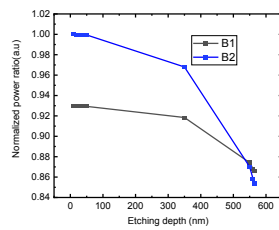Table 6. The effect of the etching cladding layer depth on the B, α, β and γ
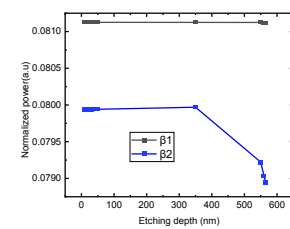
PD absorber thickness	B1, B2	α1, α2, γ1, γ2	β1, β2
5nm			
4nm			
3nm			
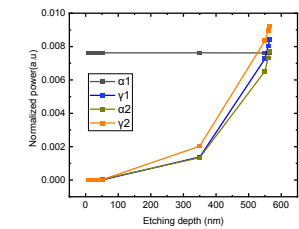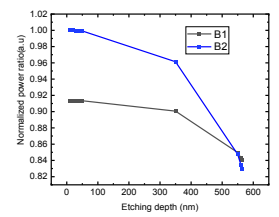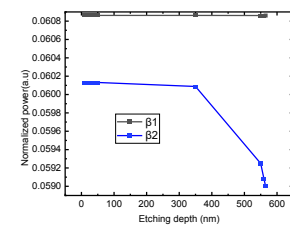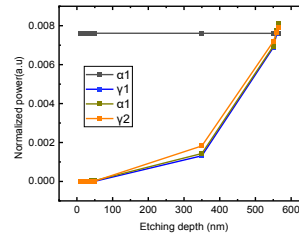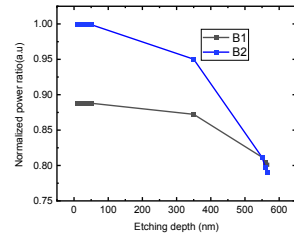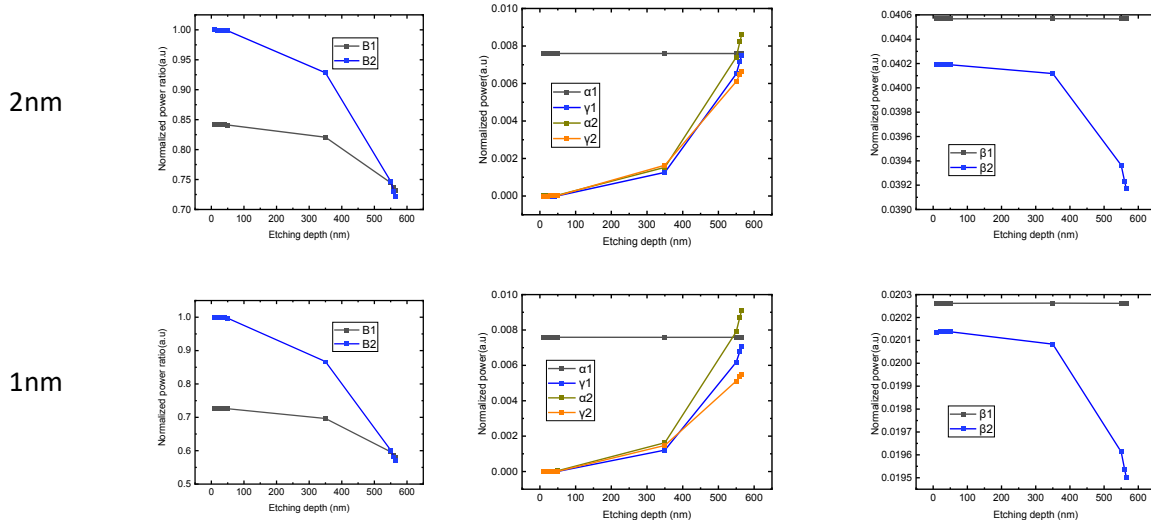
Among these factors, the most significant are α2 and γ2, which represent the general front-end loss and back-end loss, respectively, which can mainly affect the total quantum efficiency. I can plot the effect of the etching cladding layer depth on the α2 and γ2 for different PD absorber thickness.
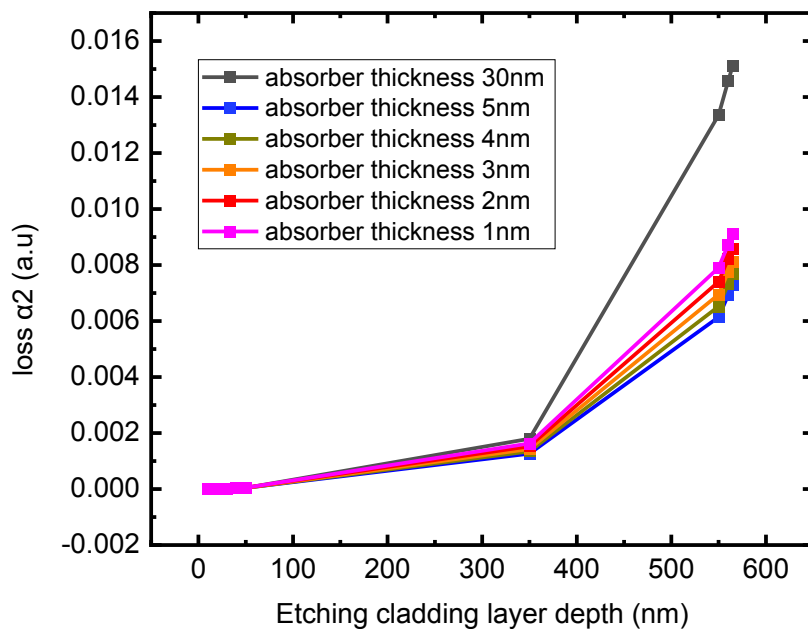
Figure 49. The effect of the etching cladding layer depth on the α2

As seen in the figures 49 and 50, it is evident that with the variation in PD absorber thickness, both the α2 and γ2 see a significant increase. Furthermore, the growth trend of the α2 with increasing thickness is more pronounced than that of the γ2. This suggests that reducing the thickness and etching the cladding layer are more effective in decreasing radiation loss at the back end than at the front end. This aligns well with the intended objective of the optimization design.
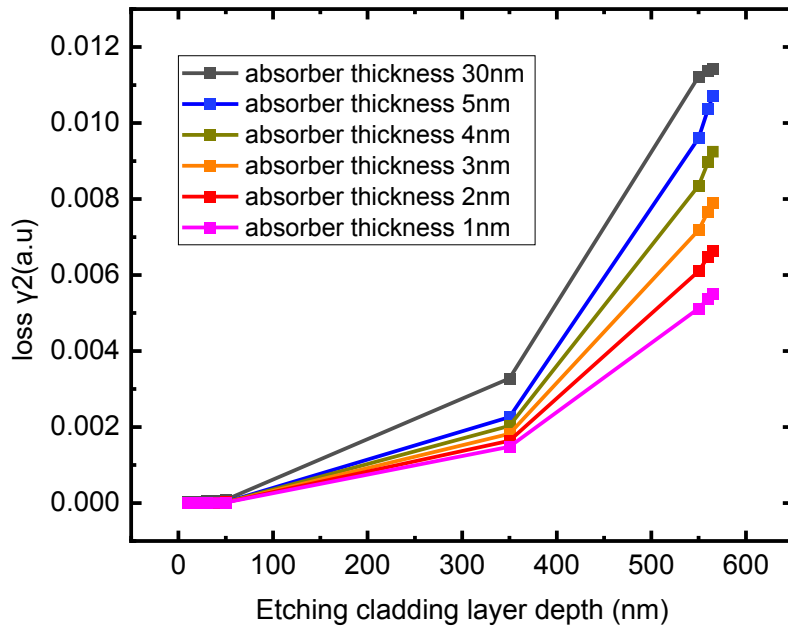
Figure 50. The effect of the etching cladding layer depth on the γ2

Building on previous optimization, I can choose the etching cladding layer depth of 50nm and the PD absorber thickness of 1nm as the optimized condition, according to the Remaining Power ratio=$(1-\delta)^N <$ 0.001, up to N=337 PDs can be accommodated. As shown in Figure 51, it can be observed that the power variation of 337 PDs indeed aligns with the calculated results.

(a)

(b)
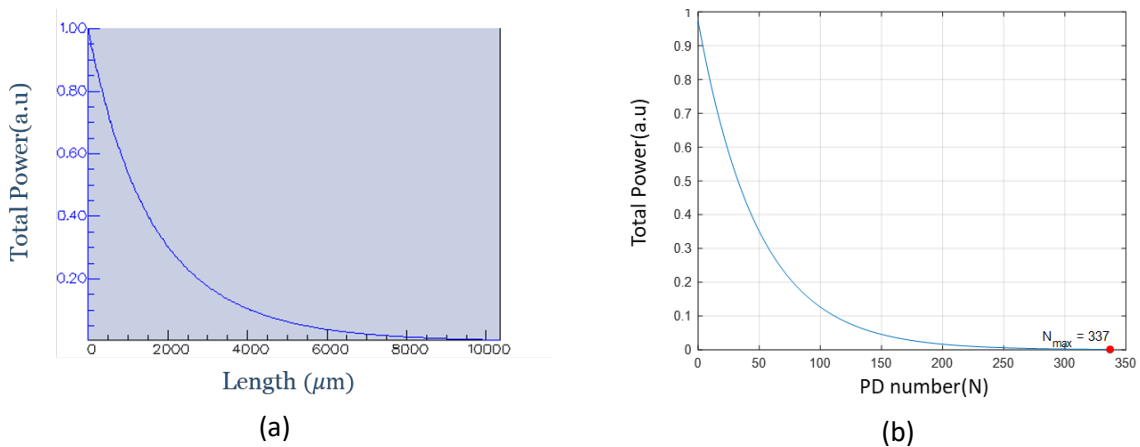
Figure 51. The variation in power of 337 PDs in relation to (a) the z-axis distance and (b) the PD number

In summary, for this case which the absorber thickness is 1nm, and etching cladding depth is 50 nm, I can obtain the α, β, and γ for the first PD and the second PD, as well as for the periodic PDs that follow,

as the table 7 shows. It should be noted that starting from the second PD onwards, all subsequent PDs should have the same parameters of the α, β, and γ.

Table 7. Parameters for the absorber thickness 1nm, and etching cladding layer depth 50 nm

α1	0.00759	α2	4.73104E-5
β1	0.02026	β2	0.02014
γ1	6.1709E-6	γ2	1.25961E-5

Since that the first PD still has a substantial left loss α1 (about 0.759%), using following formula, I can calculate the total radiation loss and the total quantum efficiency of the remaining 336 segments PDs:

$$\alpha_{\text{in}}\,(\eta_{\text{in}}) = 1 - \eta_{\text{in}} = 0.000047 \quad \rightarrow \quad \eta_{\text{in}} = 0.999953$$

$$QE = 0.02 \quad \rightarrow \quad 1 - QE = 0.98$$

$$\gamma_{\text{out}}\,(\eta_{\text{out}}) = 1 - \eta_{\text{out}} = 0.000012 \quad \rightarrow \quad \eta_{\text{out}} = 0.999988$$

Total QE

$$PD_{1\text{n}}(x+1, \eta_{\text{out}}, \eta_{\text{in}}) = PD_1 + \sum_{n=1}^{x}\left[\left(T(\eta_{\text{out}}, \eta_{\text{in}})\right)^n \cdot (\eta_{\text{in}} \cdot QE)\right]$$

$$T(\eta_{\text{out}}, \eta_{\text{in}}, QE) = \eta_{\text{in}} \cdot (1 - QE) \cdot \eta_{\text{out}}$$

$$\rightarrow \quad PD_{1\text{n}}(336, \eta_{\text{out}}, \eta_{\text{in}}, QE) = 99.6\%$$

I can calculate the total quantum efficiency after the deployment of 337 PDs except the first PD, as illustrated in the figure 52. The outcome reveals that the total quantum efficiency of the 336 photodetectors amounts to 99.6%, a notably elevated value that closely approaches 100%, which is already quite high, suggesting this outcome serves as compelling evidence that that my optimization endeavors have been highly successful.
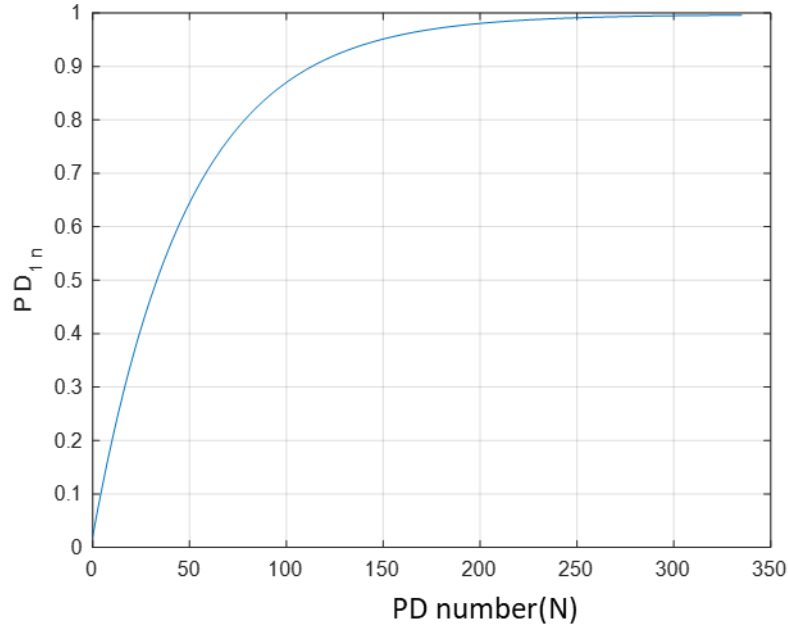
Figure 52. The total QE versus the 337 segment PDs except the first PD

I can also calculate the total radiation loss and the remaining power of the 337 segments PDs except the first PD:

Total radiation loss

$$\text{Loss}\left(\eta_{\text{in}}, \eta_{\text{out}}, \text{QE}, x\right)$$
$$= \alpha_{\text{in}}\left(\eta_{\text{in}}\right) + \left[\eta_{\text{in}} \cdot (1 - \text{QE}) \cdot \gamma_{\text{out}}\left(\eta_{\text{out}}\right)\right]$$
$$+ \sum_{m=1}^{x}\left[\eta_{\text{in}} \cdot \text{T}(\eta_{\text{out}}, \eta_{\text{in}}, \text{QE})^{n} \cdot (1 - \text{QE}) \cdot \gamma_{\text{out}}\left(\eta_{\text{out}}\right)\right]$$
$$+ \left(\text{T}(\eta_{\text{out}}, \eta_{\text{in}}, \text{QE})^{m} \cdot \alpha_{\text{in}}\left(\eta_{\text{in}}\right)\right)\right]$$

➤ $\text{Loss}(\eta_{\text{in}}, \eta_{\text{out}}, QE, 336) = 0.29\%$

Remaining power

$$\text{Powerleft}\left(x, \eta_{\text{in}}, \eta_{\text{out}}, QE\right) = 1 - \text{Loss}\left(\eta_{\text{in}}, \eta_{\text{out}}, QE, x\right) - \text{PD } 10(x, \eta_{\text{out}}, \eta_{\text{in}}, QE)$$

➤ $\text{Powerleft}\left(336, \eta_{\text{in}}, \eta_{\text{out}}, QE\right) = 0.11\%$

As shown in the figure 53, the curves depicting the variation of total quantum efficiency, total loss, and left power as a function of the number of PDs can be observed. Similarly, I can read the final values of various parameters after passing through the 337 PDs except the first PD from this figure.
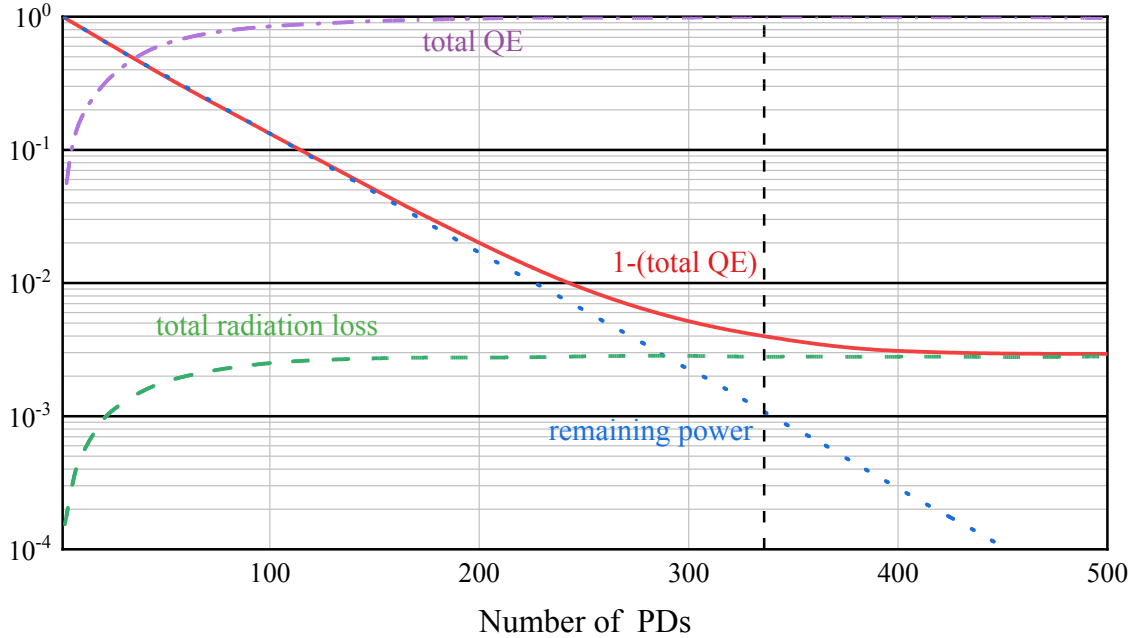
54

Figure 53. The curves for total QE, total loss, etc., versus the 337 segment PDs except the first PD

After the calculation, the total radiation loss of the remaining 336 PDs is only 0.29%. At this point, this is the best result achieved through optimization in this thesis. Especially noteworthy is the fact that after passing through 336 PD cycles, the total radiation loss is still only 0.29%, which is quite remarkable.

The total radiation loss 0.29% (total QE 99.6%) is significantly better than the 7% total radiation loss result (total QE 93%) obtained by Qianhuan. The primary reason is that the number of PDs which is 337 is much greater than his 50. This is mainly due to reducing both α2 and γ2 to the level of 10^{-5}(0.001%) so that it can lead the total radiation loss only 0.29%, which are extremely minimal losses that can essentially be disregarded. In summary, this represents a significant optimization of the segmented waveguide photodetector system, and this optimization can be leveraged to further improve the device and explore potential applications in quantum information processing and quantum communication.

Chapter 5. Conclusion

The research conducted in this study focused on the development and analysis of a segmented waveguide photodetector, with a specific emphasis on its potential applications in quantum measurements, particularly photon number resolution. The key findings of this study can be summarized as follows:

- Through simulations, the segmented waveguide photodetector has been demonstrated to exhibit very low loss, suggesting its potential for applications that require PNR and high QE.

- High Quantum Efficiency: Through design optimization and in-depth analysis, the photodetector achieved high quantum efficiency (QE), making it a potential candidate for precise photon number resolution tasks within quantum measurements.

- Optimization through Finite Element Method: The utilization of the finite element method enabled precise modeling and simulation of the photodetector, allowing for the fine-tuning of the device's design including absorber thickness and cladding etch depth, to maximize its performance.

- Radiation Loss Reduction: Detailed analysis of quantum efficiency and incorporating the main loss mechanisms led to insights into performance trade-offs and optimization mechanisms. Through optimization efforts, each radiation loss was minimized to an exceptional level of 10^{-5}, This optimization significantly bolstered the total quantum efficiency of the segment PDs system (the total quantum efficiency of the 337 photodetectors except the first PD is 99.6%), accommodating up to 337 PDs, and with a mere 0.29% total radiation loss except the first PD, far surpassing the previous records.

In conclusion, this study represents a significant step forward in the design and simulation of segmented waveguide photodetectors characterized by high quantum efficiency.

Chapter 6. Future Work

The future work involves addressing certain additional loss mechanisms that have not been accounted for in the current analysis. These include the waveguide losses attributed to material loss, specifically between segment photodiodes and the loss in metal contacts.

To comprehensively assess the system's efficiency, future endeavors should incorporate these additional loss mechanisms, encompassing waveguide and metal losses, as well as any other pertinent factors that may contribute to the total loss. The subsequent step involves recalibrating the model to ascertain the practical loss and the total quantum efficiency, laying the groundwork for a more accurate representation of the system. This refined model can then be applied to the design and optimization of segment waveguide Single Photon Avalanche Diodes (SPADs).

Additionally, there are several potential ideas that can be implemented.

6.1 Taper PD on waveguide

The transmission from the passive waveguide to the absorbing layer presents challenges due to the shift from single mode to a supermode consisting of odd and even modes. This shift results in a significant change in effective refractive index or propagation constants, leading to substantial radiation losses. To address this issue, I draw inspiration from UCSB's design of the evanescent quantum dot laser on Si, as the figure 54 shows, and introduce the concept of the taper PD on the waveguide.
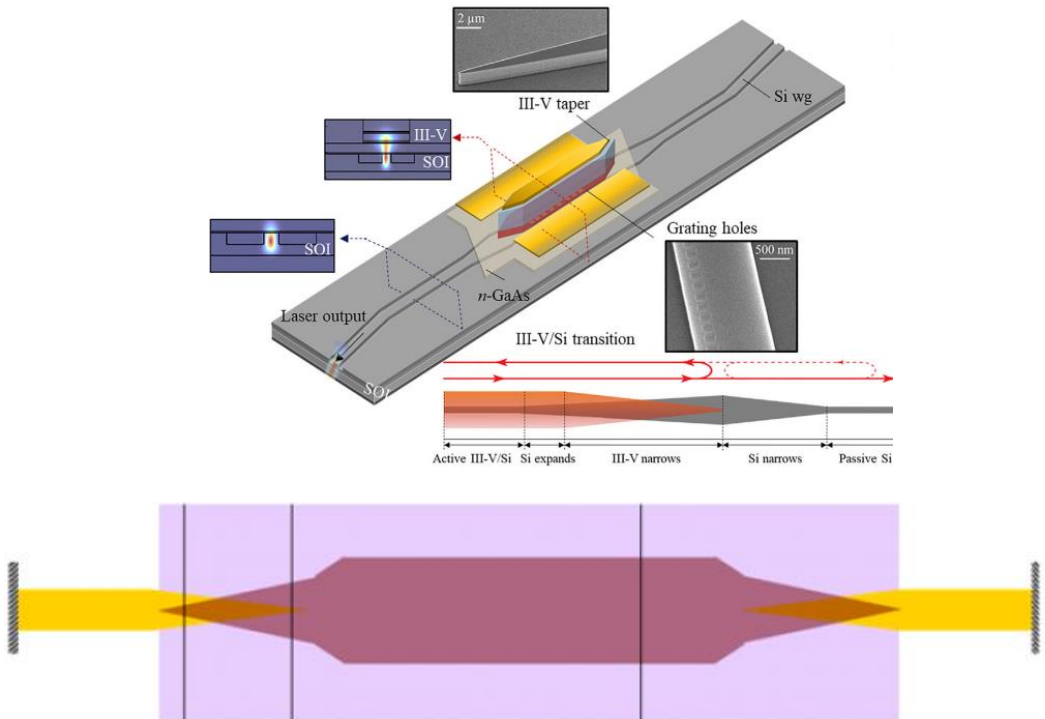
Figure 54. (a)Schematic image of the evanescent QD laser on Si (b)Top view of the III-V/SOI laser by UCSB[29]

The Taper PD on waveguide involves tapering the absorbing layer at both ends, gradually varying its size to create a smooth change in effective refractive index or propagation constants. This design allows the tapered region to match the properties of the passive waveguide, while the central part retains the original characteristics of the absorbing layer. Two design options are considered: one maintains the size of the passive waveguide unchanged, while the other gradually reduces the size of the passive waveguide at the junction to match the absorbing layer, as the figure 55 shows.

(a)

(b)
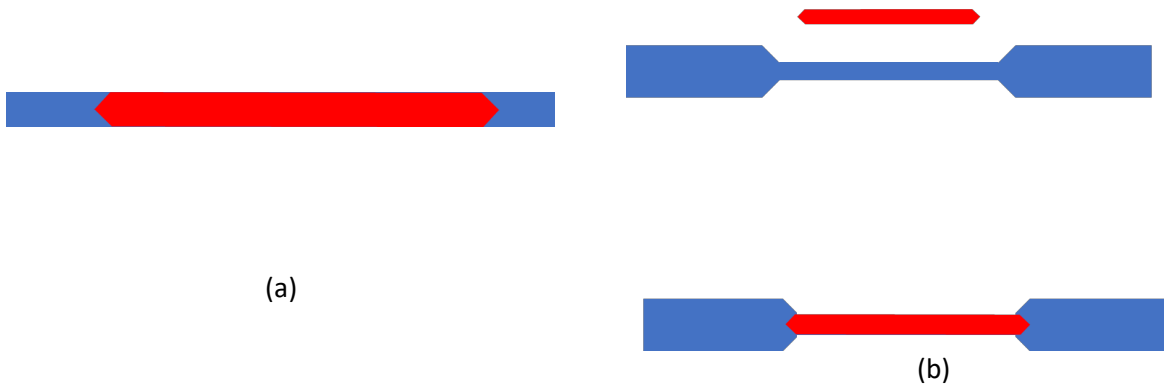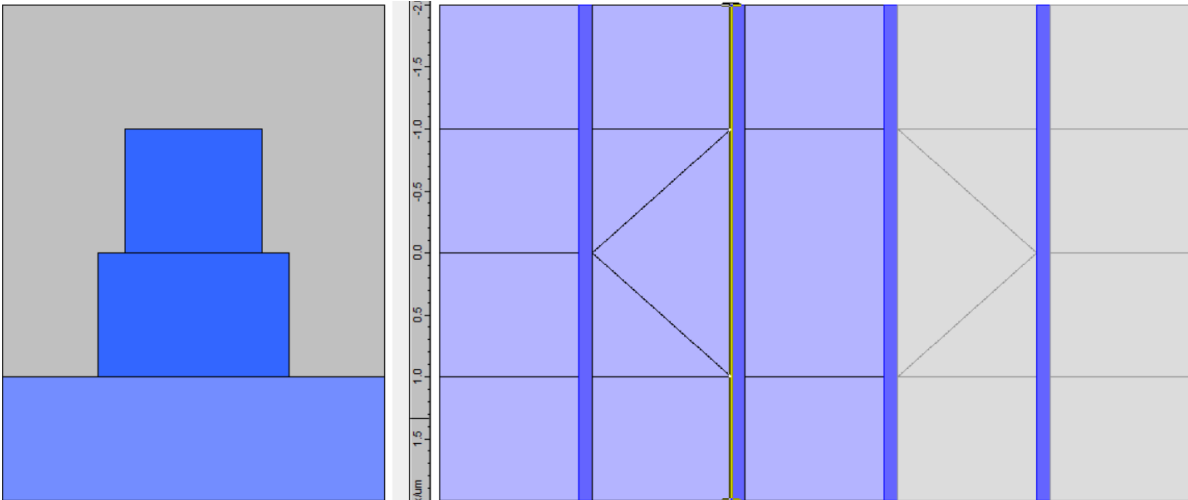
(c)

Figure 55. Schematic image of (a) Taper PD on the unchanged passive waveguide (b) Taper PD on the reverse taper passive waveguide (c) Actual simulation diagram from FIMMWAVE of Taper PD on the unchanged passive waveguide

6.2 Further optimization of the device structure

The future optimization of the device structure holds promising potential for enhancing the performance of the photodetector. One approach involves adjusting the orientation of the PD and the passive waveguide. For instance, placing the PD and passive waveguide on the same horizontal plane within the same substrate, parallel to each other, with an intermediate cladding layer, can be explored. This arrangement ensures that the coupling between the passive waveguide and the PD occurs in the horizontal direction rather than the vertical interface direction in the previous structure.

Taking inspiration from directional couplers, S-bend structures at the connection points can be employed to reduce radiation losses during the coupling between the passive waveguide and the PD. This approach can further improve the total QE and enhance the overall performance of the system.

Moreover, other design concepts, such as multimode interference (MMI), optical gratings, and metasurfaces, can also be investigated to boost the total QE and overall system performance. By leveraging these innovative approaches, the device's performance can be significantly improved, making it more suitable for various applications. In addition to the current use of the directional coupler principle, one can also try the structural principle of the adiabatic coupler, as the figure 56 shows.
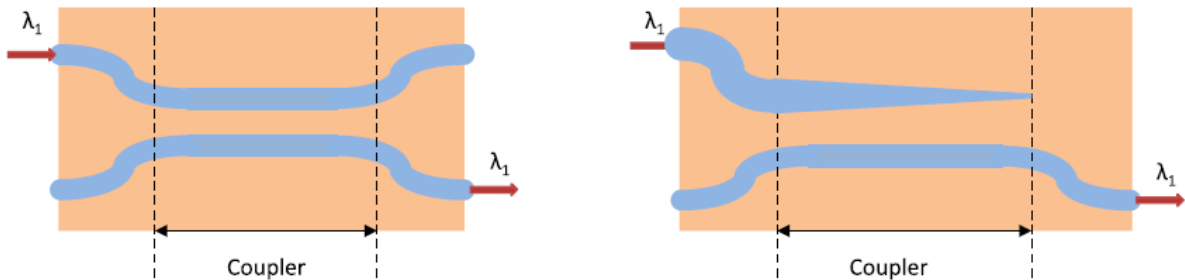

Figure 56. Schematic representation of a directional coupler (on the left) and of an adiabatic coupler (on the right) [30]

In conclusion, further optimization of the photodetector's device structure, including the PD and passive waveguide arrangement, incorporation of S-bend structures, and exploration of MMI, optical gratings, and metasurfaces, holds great promise in improving quantum efficiency and the overall performance of the photodetector system. Additionally, careful material selection can help mitigate losses originating from the passive waveguide, contributing to the enhancement of the device's performance.

6.3 Further optimization of fabrication

The pursuit of further optimization in fabrication techniques holds immense potential for minimizing losses in photodetector devices. One promising avenue for achieving this objective involves the adoption of the well-established Damascus Process, renowned for its capacity to substantially reduce losses in optical waveguides.

It's worth noting that additional losses originating from the passive waveguide (WG1) can be mitigated by the strategic selection of low-loss materials. For instance, Si_3N_4 waveguides, boasting a loss rate of 0.1 dB/cm [27], or InGaAsP waveguides with a loss of 0.4 dB/cm [28], offer opportunities to diminish these losses. By judiciously choosing materials and engineering the device structure, these losses can be significantly curtailed, thereby elevating the overall system's performance.

Harnessing the benefits of the Damascus Process may enable the further reduction of losses within these waveguides, leading to marked enhancements in the photodetector's overall performance. The reduction of losses within the waveguide is pivotal, as it directly impacts light transmission efficiency, thereby influencing the sensitivity and total quantum efficacy of the photodetector device.

Sustained research and development efforts in fabrication techniques, exemplified by the Damascus Process, hold the potential to unlock new frontiers in high-performance photodetector devices with even lower losses, heightened quantum efficiency, and enhanced photon number resolution. This advancement has the potential to usher in more efficient photodetectors, catering to applications across diverse domains, encompassing optical communications, quantum technologies, medical imaging, and beyond. As the field of photonics continues to evolve, optimizing fabrication processes remains pivotal in realizing the full potential of photodetector technologies.

6.4 Further optimization of applications

The potential for further optimization of photodetector structures, including Single-Photon Avalanche Diodes (SPADs) and Avalanche Photodiodes (APDs), opens exciting opportunities for advancing their applications, especially in the domain of photon number resolution.

SPADs represent a promising class of devices with the unique capability to detect single photons, offering both high quantum efficiency and ultrafast response times. Operating in Geiger mode, SPADs leverage the principle that a single photon triggers an avalanche of charge carriers, resulting in a detectable electrical signal. Their versatility has led to widespread use in various fields, including quantum key distribution, time-of-flight measurements, and quantum imaging.

In contrast, APDs are semiconductor-based devices that employ a different operation al mode compared to SPADs. They, too, facilitate photon counting and can achieve heightened sensitivity compared to traditional photodiodes. APDs harness the avalanche effect to amplify the photocurrent, making them well-suited for low-light-level applications such as fluorescence spectroscopy and lidar.

Exploring diverse SPAD and APD structures holds the potential for creating more adaptable and high-performance photodetectors tailored for photon number resolution applications. Innovative material combinations and engineering strategies may yield enhancements in quantum efficiency, noise reduction, and counting capabilities, driving forward the development of advanced photodetector technologies.

References

[1] Yu, Q., Sun, K., Li, Q. and Beling, A., 2018. Segmented waveguide photodetector with 90% quantum efficiency. Optics express, 26(10), pp.12499-12505.

[2] Nehra, R., Chang, C.H., Yu, Q., Beling, A. and Pfister, O., 2020. Photon-number-resolving segmented detectors based on single-photon avalanche-photodiodes. Optics Express, 28(3), pp.3660-3675

[3] https://www.rp-photonics.com/photodiodes.html

[4] https://www.fiberoptics4sale.com/blogs/wave-optics/avalanche-photodiodes

[5] Yuan, Y., 2019. Low-Noise Avalanche Photodiodes.

[6] Chunnilall, C.J., Degiovanni, I.P., Kück, S., Müller, I. and Sinclair, A.G., 2014. Metrology of single-photon sources and detectors: a review. Optical Engineering, 53(8), pp.081910-081910.

[7] Abdullah, Salman. (2019). Avalanche Breakdown Characteristics of Thin Al0.85Ga0.15As0.56Sb0.44 Avalanche Photodiodes. 10.13140/RG.2.2.27899.23844.

[8] https://www.nist.gov/pml/quantum-networks-nist/technologies-quantum-networks/single-photon-detectors

[9] Signorelli F, Telesca F, Conca E, , et al. Low-noise InGaAs/InP single-photon avalanche diodes for fiber-based and free-space applications[J]. IEEE Journal of Selected Topics in Quantum Electronics, 2021, 28(2): 1-10.

[10] https://en.wikipedia.org/wiki/Superconducting_nanowire_single-photon_detector.

[11] GOL'Tsman G N,Okunev O, Chulkova G, et al. Picosecond superconducting single-photon optical detector [J]. Applied Physics Letters,2001,79(6) :705 - 707.

[12] Hadfield R H. Single-photon detectors for optical quantum information applications [J] . Nature Photonics, 2009, 3 (12): 696-705.

[13] Natarajan, Chandra M, et al. Superconducting nanowire single-photon detectors: physics and applications [J]. Superconductor Science and Technology, 2012, 25 (6) :63001.

[14] Esmaeil Zadeh I, Chang J, Los J W N, et al. Superconducting nanowire single-photon detectors: a perspective on evolution, state-of-the-art, future developments, and applications [J]. Applied Physics Letters, 2021, 118 (19): 190502.

[15] https://en.wikipedia.org/wiki/Transition-edge_sensor

[16] Dauler, E.A., Kerman, A.J., Robinson, B.S., Yang, J.K., Voronov, B., Goltsman, G., Hamilton, S.A. and Berggren, K.K., 2009. Photon-number-resolution with sub-30-ps timing using multi-element superconducting nanowire single photon detectors. Journal of Modern Optics, 56(2-3), pp.364-373.

[17] Robert H. Hadfield, Jonathan Leach, Fiona Fleming, Douglas J. Paul, Chee Hing Tan, Jo Shien Ng, Robert K. Henderson, and Gerald S. Buller, "Single-photon detection for long-range imaging and sensing," Optica 10, 1124-1141 (2023)

[18] https://www.photonics.com/Articles/By_the_Numbers_Photon_Counting_and_Number/a68893

[19] Beling, A., 2006. Periodic travelling wave photodetectors with serial and parallel optical feed based on InP.

[20] https://www.fiberoptics4sale.com/blogs/wave-optics/directional-couplers

[21] Kivshar, Y.S. and Agrawal, G.P., 2003. Optical solitons: from fibers to photonic crystals. Academic press.

[22] L. U. Kibler, "The cutoff region of a rectangular waveguide with losses, its properties and uses," in The Bell System Technical Journal, vol. 48, no. 7, pp. 2221-2258, Sept. 1969, doi: 10.1002/j.1538-7305. 1969.tb01171.x.

[23] https://www.ece.mcmaster.ca/faculty/bakr/ECE757/PMLlecture_Berenger.pdf

[24] https://www.photond.com/products/fimmwave/fimmwave_features_20.htm

[25] Gallagher, D.F., and Felici, T.P., 2003, June. Eigenmode expansion methods for simulation of optical propagation in photonics: pros and cons. In Integrated optics: devices, materials, and technologies VII (Vol. 4987, pp. 69-82). SPIE.

[26] Dosunmu, O.I., Cannon, D.D., Emsley, M.K., Ghyselen, B., Liu, J., Kimerling, L.C. and Unlu, M.S., 2004. Resonant cavity enhanced Ge photodetectors for 1550 nm operation on reflecting Si substrates. IEEE Journal of selected topics in quantum electronics, 10(4), pp.694-701.

[27] P. Munoz, P. W. van Dijk, D. Geuzebroek, M. Geiselmann, C. Dominguez, A. Stassen, J. D. Doménech, M. Zervas, A. Leinse, C. G. H. Roeloffzen, B. Gargallo, R. Baños, J. Fernández, G. M. Cabanes, L. A. Bru, and D. Pastor, "Foundry developments toward silicon nitride photonics from visible to the mid-infrared," IEEE J. Sel. Top. Quantum Electron. 25(5), 1–13 (2019).

[28] D. D'Agostino, G. Carnicella, C. Ciminelli, P. Thijs, P. J. Veldhoven, H. Ambrosius, and M. Smit, "Low-loss passive waveguides in a generic inp foundry process via local diffusion of zinc," Opt. Express 23(19), 25143–25157 (2015).

[29] Wan, Y., Xiang, C., Koscica, R., Kennedy, M.J., Huang, D., Gossard, A.C. and Bowers, J.E., 2022, May. 1.3 μm High Speed Heterogeneous Quantum-Dot Lasers on Si. In CLEO: Science and Innovations (pp. SM2P-1). Optica Publishing Group.

[30] Grigorij Muliuk., 2020. Micro-Transfer-Printing of III-V Semiconductor and Silicon-Germanium Photodetectors on Silicon Photonic Integrated Circuits.